Direct Population and Lifetime Measurements of the 2_1^+ and 4_1^+ States in ^{40}Ca Using an Alpha-Transfer Reaction

by

Tongan Wu

B.Sc., Simon Fraser University, 2019

Thesis Submitted in Partial Fulfillment of the
Requirements for the Degree of
Master of Science

in the
Department of Chemistry
Faculty of Science

Declaration of Committee

Name: **Tongan Wu**

Degree: **Master of Science**

Thesis title: **Direct Population and Lifetime Measurements of the 2_1^+ and 4_1^+ States in ^{40}Ca Using an Alpha-Transfer Reaction**

Committee: **Chair:**   Paul Li
Professor, Chemistry

Krzysztof Starosta
Supervisor
Professor, Chemistry

Loren Kaake
Committee Member
Associate Professor, Chemistry

Greg Hackman
Committee Member
Research Scientist, TRIUMF

Corina Andreoiu
Examiner
Professor, Chemistry

Abstract

At TRIUMF, Canada's particle accelerator centre, the TIGRESS Integrated Plunger (TIP) and its configurable detector systems have been used for charged-particle tagging and light-ion identification in Doppler-shift lifetime measurements using gamma-ray spectroscopy with the TIGRESS array of HPGe detectors. An experiment using these devices to measure the lifetime of the 2_1^+ and 4_1^+ states of ^{40}Ca has been performed by projecting an ^{36}Ar beam onto a $^{nat.}$C target. Analysis of the experimental gamma-ray spectra confirmed the direct population of these states. Kinematics of the reaction mechanism were identified using Monte-Carlo simulations, which also enabled the use of charged-particle correlations to select reactions that populated a specific excited state in the ^{40}Ca immediately after its production. Selection of the 2_1^+ state with this additional sensitivity further eliminated feeding cascades, and therefore restricted the decay kinetics predominantly to first order. Direct population of the 2_1^+ state was achieved with a direct-population-to-feeding ratio of $21(\pm2) : 1$. The 2_1^+ lifetime that was measured in this experiment was 42 ± 5 fs, and the 4_1^+ lifetime was 270 ± 10 fs. Both uncertainties quoted here are statistical only.

Keywords: ^{40}Ca; Lifetime measurement; DSAM; transfer reaction

Acknowledgements

First, I would like to thank my undergraduate and MSc. supervisor Dr. Kris Starosta for his support, guidance, and patience over the years. I would also like to thank my committee members Dr. Loren Kaake and Dr. Greg Hackman for their advice and encouragements. Dr. Phil Voss, Dr. Corina Andreoiu, and Dr. Pietro Spagnoletti also provided very valuable insights that are included in this thesis.

The work that is described in this thesis was a result of an experiment that was performed by many collaborators in the TIP-TIGRESS collaboration at TRIUMF and SFU. This thesis would not be possible without them.

Sorting and analyzing data from TIP and TIGRESS required a long learning curve. Therefore I am very grateful for my former and current colleagues in the Starosta Lab: Dr. Aaron Chester, Dr. Jonathan Williams, (maybe a Dr. now?) Thomas Domingo, Andrew Redey, Matt Martin, Heinz Asch. Thank you for your help and for answering all my endless questions.

In addition to the names already listed, I would also like to thank all the colleagues that I have worked and hung out with at SFU over the years for the many lunches and interesting conversations we had together. In particular, I would like to thank Dr. Fatima Garcia for convincing me to try volleyball, Melanie Gascoine for her impressions of Kris, Dr. Nas Yousefi for her infectious laughs, Dr. Luiza Gomez for going to the volleyball training camps with me, Dr. Kenneth Whitmore for his weekly puzzles, Kevin Ortner for his dad jokes, and Isaiah and Sydney for trusting me with their lives.

Finally, and most importantly I would like to thank my parents Wu Lixin and Yi Jingwei for their continued moral and financial support, and my husband Elizer for always being there for me and editing this thesis.

Table of Contents

List of Figures

Chapter 1

Introduction

The effective nuclear force governs the interactions between protons and neutrons in an atomic nucleus as a result of the strong force between their constituent quarks. An illustration of these forces is shown in Figure 1.1. The two forces are analogous to the Van der Waals force [1] between molecules and the Coulomb force between atoms, where the latter is known to determine the former. Just as the Van der Waals force determines the equation of state of a molecular gas, the effective nuclear force is expected to provide the same insight on the nucleon-nucleon interactions in atomic nuclei.
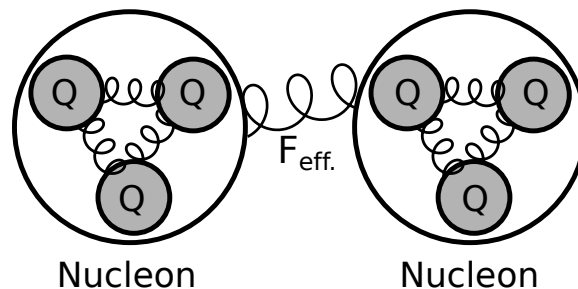
Figure 1.1: The strong force holds together the quarks (Q) in a nucleon. The manifestation of the strong force, the effective nuclear force ($F_{\text{eff.}}$), holds together nucleons.

However, the derivation of the effective nuclear force from the strong force is yet to be established. While recent developments in Quantum Chromodynamics (QCD)-inspired theories [2, 3] contribute to making this connection with ab-initio predictions in low-to-medium mass nuclei, they still need to be rigorously tested against experimental data. The doubly-magic [4] ^{40}Ca$(N = Z = 20)$ is a popular testing ground for these nuclear structure theories because both its proton and neutron shells are fully occupied. These full nuclear shells are analogous to the full electron shells in noble gases, as they provide the system with extra stability.

1.1 ^{40}Ca Lifetime as a Probe for the Effective Nuclear Force

One key observable in ^{40}Ca that is used to examine nuclear structure theories is the lifetimes of its excited 2_1^+ and 4_1^+ states[1]. This is because the lifetimes can be calculated from the wavefunctions of the nuclear states, which are predicted by the theories and the well-understood electric quadrupole ($E2$) operator. The 4_1^+ state decays to the 2_1^+ state, and the 2_1^+ decays to the 0_1^+ ground state. The $4_1^+ \rightarrow 2_1^+$ and $2_1^+ \rightarrow 0_1^+$ are both electric quadrapole transitions. For an electric quadrapole transition, the transition rate from an initial state with angular momentum J_i, to a final state with angular momentum J_f, is given by [5]:

$$T_{J_i \rightarrow J_f, E2} = \left(\frac{12\pi}{225} \right) \left(\frac{k^5}{\hbar} \right) B(E2; J_i \rightarrow J_f) \, , \tag{1.1}$$

where k is the wavenumber of the transition with energy E_γ, given by:

$$k = \frac{E_\gamma}{\hbar c} = \frac{E_\gamma}{197 \text{ MeV fm}} \, , \tag{1.2}$$

and $B(E2; J_i \rightarrow J_f)$ is the reduced electric quadrupole transition probability given by:

$$B(E2; J_i \rightarrow J_f) = \frac{\langle J_f ||E2|| J_i \rangle^2}{2J_i + 1} \, , \tag{1.3}$$

where $\langle J_f ||E2|| J_i \rangle$ is the reduced matrix element that is calculated from the wavefunctions of the initial and final states, $|J_i\rangle$ and $\langle J_j|$, and the electric quadrupole operator $E2$. Finally, lifetime of this transition, $\tau_{J_i \rightarrow J_f}$, is given by:

$$\tau_{J_i \rightarrow J_f} = \frac{1}{T_{J_i \rightarrow J_f, E2}}, \propto \left[E_\gamma^5 \, B(E2; J_i \rightarrow J_f) \right]^{-1} . \tag{1.4}$$

As a result, accurate and precise lifetime measurements can be used to validate the quality of the QCD-inspired *ab-initio* theories by comparing the lifetimes they calculate to the experimental values. In addition, the experimentally-determined lifetimes will also provide empirical models, such as the nuclear shell model [6], with a more steady foundation to fit their parameters which will allow them to make better predictions of the more exotic nuclei farther from stability.

However, current experimental measurements of the 2_1^+ and 4_1^+ lifetimes each have large uncertainties of 20% [7]. This precision is insufficient to distinguish the merit between different theories while also limiting the predictive power of the phenomenological models

---

[1]The notation J_n^π is used to indicatate the nth state with angular momentum J and parity π. Selection rules for gamma decays can be found in Section 4.4 in Ref. [5]

that are derived from fits on experimental data around magic number nuclei. Section 1.2 discusses the existing measurements in more detail.

1.2 Literature Review

1.2.1 Lifetimes

Since the magic numbers were identified by Mayer [8][2] in 1948, the doubly-magic ^{40}Ca has been a textbook nucleus for theoretical predictions [9]. For this reason, there has been keen interest in the measurement of its properties. One such property is the lifetime of its 2_1^+ excited state. This is because the lifetime provides a bridge between experimental observations and nuclear structure theories [9], as described in Section 1.1. A summary of the previously measured 2_1^+ lifetime of ^{40}Ca, together with calculations from selected modern theories, is shown in Figure 1.2.
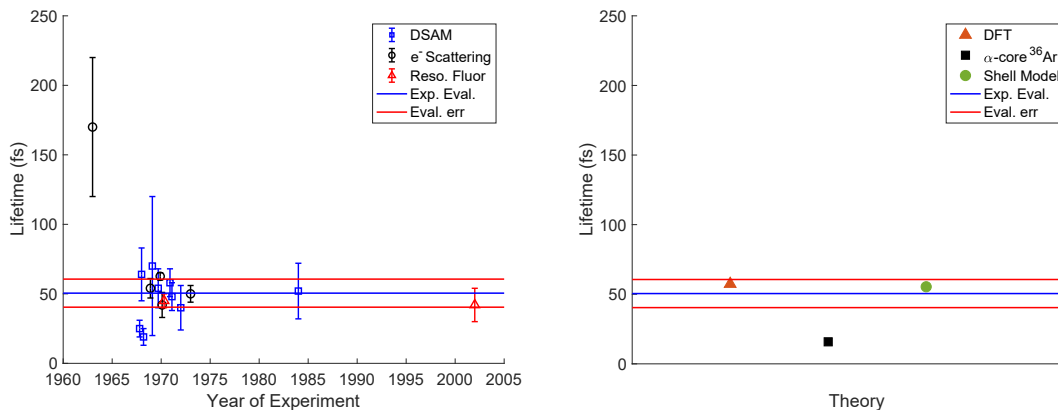
Figure 1.2: Markers: lifetime of the 2_1^+ excited state in ^{40}Ca from previous experiments (left) and theoretical calculations (right). Lines: evaluated lifetime from the experiments. The values were taken from Ref. [7] for experiments and Ref. [10] for theories.

The measurements were mostly performed in the 1960s and 1970s with large uncertainties. Among them, the few higher-precision measurements do not agree with one another. Although there was a more recent measurement from 2002 [11], its uncertainties were too large to resolve the discrepancies between previous measurements. As a result, the evaluated experimental 2_1^+ lifetime for ^{40}Ca had large uncertainties of 20% [7], making it difficult to discriminate the quality between the different theories. One reason that these measurements had large uncertainties was the effect of feeding, which is discussed in Section 2.2. Traditional techniques, such as fusion-evaporation [12], tend to populate high-energy states. As a result, feeding will almost always be present to limit precise lifetime measurements of the

---

[2]Nuclei with magic number of protons and/or neutrons have closed nuclear shells similar to the closed electron shells in noble gases.

lower-lying states. The alpha-transfer reaction mechanism, described in Section 1.2.2, can be used to eliminate feeding by populating the lower-lying states directly.

The literature values for the ^{40}Ca's 4_1^+ lifetime is similar to that of the 2_1^+. Its evaluated experimental lifetimes [7] of 300 ± 60 fs also has a 20% uncertainty. Previous measurements of the 4_1^+ lifetime is shown in Figure 1.3.
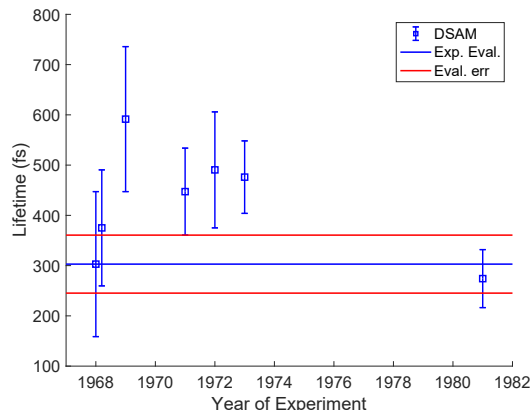
Figure 1.3: Markers: lifetime of the 4_1^+ excited state in ^{40}Ca from previous experiments. Lines: evaluated lifetime from the experiments. The values were taken from Ref. [7].

1.2.2 Reaction Mechanism

Sub-barrier alpha-transfer reaction is a powerful but under-explored mechanism for probing low-lying excited states in ^{40}Ca. Alpha-transfer reactions with inverse kinematics on ^{12}C targets, where the heavier beam picks up an alpha cluster from the ^{12}C target, with beam energies close to the Coulomb barrier have been used for lifetime measurements in other nuclei such as ^{110}Sn [13], and various Kr [14] and Zn [15] isotopes. The reaction mechanism has also been used to populate isotopes as heavy as ^{100}Pd in magnetic moment studies [16]. In these experiments, the alpha-transfer reaction was used to selectively populate low-lying excited nuclear states, such as 2_1^+ and 4_1^+. Measurements using this reaction mechanism were "proven to be coherent and robust", but the reaction mechanism was "not yet well described and even less understood" [14]. Ref. [14] observed that the alpha-transfer reaction was "resonance-like" for energies close to the Coulomb barrier: Coulomb excitation[3] dominates reactions at energies below the barrier while fusion-evaporation[4] dominates at higher energies. They also reported that the relative yield of the alpha-transfer reaction with respect to the Coulomb excitation of the beam was decreased as the beam energy

---

[3]Coulomb excitation: exciting a nucleus to a higher nuclear state via the Coulomb interaction.

[4]Fusion-evaporation: the beam and target nuclei fuse and evaporate particles after reaching thermal equilibrium. More detailed descriptions of Coulomb excitation and fusion-evaporation can be found in Chapter 3 of Ref. [17].

increased above the Coulomb barrier. However, none of the studies that are mentioned above focused on sub-barrier alpha-transfer reactions. There was also no literature [7] on populating excited states in ^{40}Ca using this reaction mechanism.

Chapter 2

Background and Techniques

2.1 The Sub-Barrier Alpha-Transfer Reaction

The reaction that is described in this thesis is from 63 MeV ^{36}Ar beam on stationary $^{\text{nat.}}$C target. This section will focus on the reaction mechanism, while detailed description of the experimental setup can be found in Chapter 3.

The Coulomb barrier between the beam and target nuclei was approximated to be the Coulomb potential at distance R_C:

$$V_C = V(R_C) = ke^2 \frac{Z_B Z_T}{R_C} \ , \tag{2.1}$$

where k is the electromagnetic coupling constant, e is the elementary charge, and Z_B, Z_T are the atomic numbers of the beam and target nuclei. R_c is the sum of the beam and target nuclei plus 2 fm:

$$R_C = R_B + R_T + 2 \text{ fm} = 1.2 \text{ fm} \left(\sqrt[3]{A_B} + \sqrt[3]{A_T} \right) + 2 \text{ fm} \ , \tag{2.2}$$

where R_B and R_T, the radii of the beam and target nuclei, are approximated by:

$$R = 1.2 \sqrt[3]{A} \ [\text{fm}] \ , \tag{2.3}$$

with A being the mass number. Combining Equations 2.1 and 2.2 the Coulomb barrier becomes

$$V_c = ke^2 \frac{Z_B Z_T}{1.2 \text{ fm} \left(\sqrt[3]{A_B} + \sqrt[3]{A_T} \right) + 2 \text{ fm}} \ , \tag{2.4}$$

and

$$V_c = 1.44 \text{ MeV} \frac{Z_B Z_T}{1.2 \left(\sqrt[3]{A_B} + \sqrt[3]{A_T} \right) + 2} \ , \tag{2.5}$$

after substituting the physical constants. Substituting the mass and atomic numbers in Equation 2.5 by those of ^{12}C and ^{36}Ar, the Coulomb barrier for the reaction is 17.86 MeV.

The kinetic energy that was available in the centre of mass can be calculated as

$$e^{CM} = \frac{\mu v^2}{2} \; , \tag{2.6}$$

where μ is the reduced mass and v is the speed of the beam in the LAB frame. The reduced mass for the beam and target nuclei with masses m_B and m_T is

$$\mu = \frac{m_B m_T}{m_B + m_T} \; . \tag{2.7}$$

Because the beam energy is

$$E_B = \frac{m_B v^2}{2} \; , \tag{2.8}$$

substituting Equations 2.7 and 2.8 into Equation 2.6 simplifies the kinetic energy in the centre of mass to

$$e^{CM} = \frac{m_t}{m_B + m_T} E_b \; . \tag{2.9}$$

Approximating the mass ratio in Equation 2.9 with mass numbers of ^{36}Ar and ^{12}C, and substituting the 63 MeV beam energy, the kinetic energy that is available in the centre of mass is 15.75 MeV. This energy is 2.1 MeV, or 12%, below the Coulomb barrier. For this reason the reaction which produced ^{40}Ca must be a sub-barrier one. The analysis in this thesis treats the population of the 2_1^+ and 4_1^+ states in ^{40}Ca as a result from a sub-barrier alpha-transfer reaction, which is illustrated in Figure 2.1. After the reaction, both
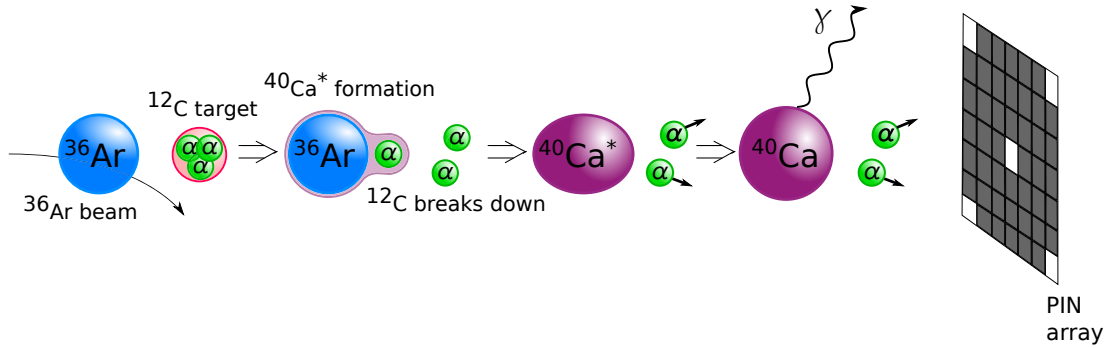
Figure 2.1: The reaction mechanism. An alpha particle tunnels from the ^{12}C to the ^{36}Ar nucleus, forming an excited ^{40}Ca (^{40}Ca*). This leaves behind an unstable 2-alpha cluster which breaks down into two alpha particles.

the ^{40}Ca* and the two alpha particles continue to travel in the direction of the beam due to the conservation of momentum. The alpha particles were detected in the PIN Array, and the ^{40}Ca* decays via emission of gamma rays which were detected in the TRIUMF ISAC Gamma Ray Suppressed Spectrometer (TIGRESS). Detailed descriptions of these detector

systems can be found in Chapter 3. Energy conservation in the centre of mass requires

$$E_{\alpha1}^{CM} + E_{\alpha2}^{CM} + E_{\text{Ca}}^{CM} + \sum E_\gamma = e^{CM} + Q \; , \tag{2.10}$$

where $E_{\alpha1}^{CM}$, $E_{\alpha2}^{CM}$, E_{Ca}^{CM} are respectively the kinetic energies of the two alpha particles and the ^{40}Ca in the centre of mass, $\sum E_\gamma$ is the total energy of all gamma rays, and Q is the energy resulted from the mass difference between the reactants and products. The Q value can be calculated as

$$Q = c^2 \left(m_{36\text{Ar}} + m_{12\text{C}} - m_{40\text{Ca}} - 2m_\alpha \right) \; , \tag{2.11}$$

where c is the speed of light, while $m_{36\text{Ar}}$, $m_{12\text{C}}$, $m_{40\text{Ca}}$, and m_α are the masses of the ^{36}Ar, ^{12}C, ^{40}Ca, and alpha particle, respectively.

2.2   The Effect of Feeding

For lifetime measurements, direct population of the state of interest is more desirable than feeding. In the context of this thesis, feeding means populating the state of interest via the decay of higher-lying state(s). If feeding is present, the measured lifetime of the state of interest becomes the combined effect of its own lifetime and the lifetimes of the higher-lying states. The general solution to successive decays are described by the Bateman equations in Ref. [18]. Extracting the lifetime of interest therefore requires knowledge of the lifetimes of those feeding states, which are not always available. Furthermore, the extracted lifetime will also inherit the uncertainties in the lifetimes of the feeding states. In contrast, if the state of interest is populated directly, the lifetime can be extracted more directly with greater precision. Figure 2.2 illustrates the difference between direct population and feeding.

2.3   Excited States in ^{40}Ca

Figure 2.3 provides a simplified level scheme of ^{40}Ca with levels that were observed in this experiment. The 4_1^+ and 0_3^+ state, if populated, will decay into the 2_1^+ state, which would then decay into the ground state. The 3_1^- state was observed, but it does not contribute to feeding of the 2_1^+ because it decays to the ground state.

2.4   Gamma-Ray Interaction with Matter

This Section introduces the interaction of gamma rays with matter to provide foundation for the lifetime measurements that are described in this thesis. The lifetimes were extracted from the line shapes of the gamma-ray spectra, which is discussed in Section 2.5.

The three types of gamma-ray interactions that affect the gamma-ray spectra are photo-electric absorption, Compton scattering, and pair production. These processes are illustrated in Figure 2.4, and described in the following Subsections.
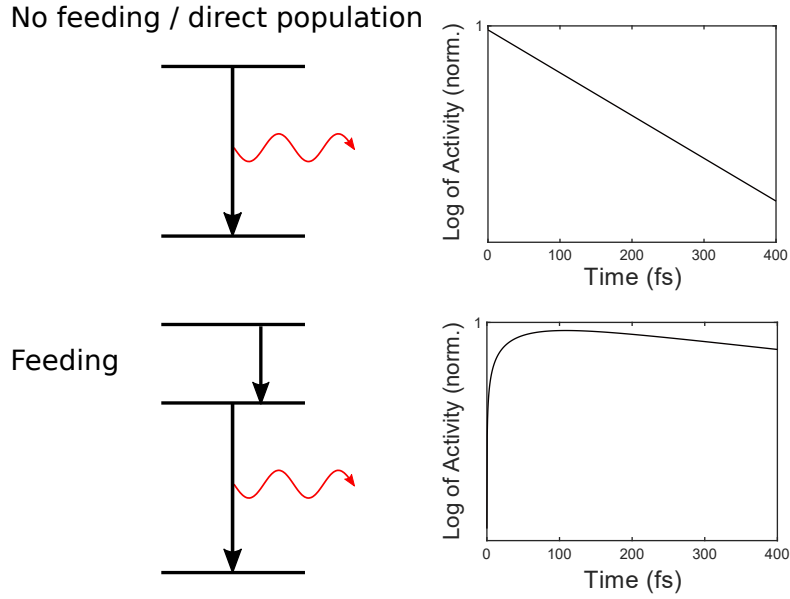
Figure 2.2: The decay kinetics of the 2_1^+ state in ^{40}Ca with (top) and without (bottom) feeding from the 4_1^+ state. The plot was generated with lifetimes from Ref. [7].
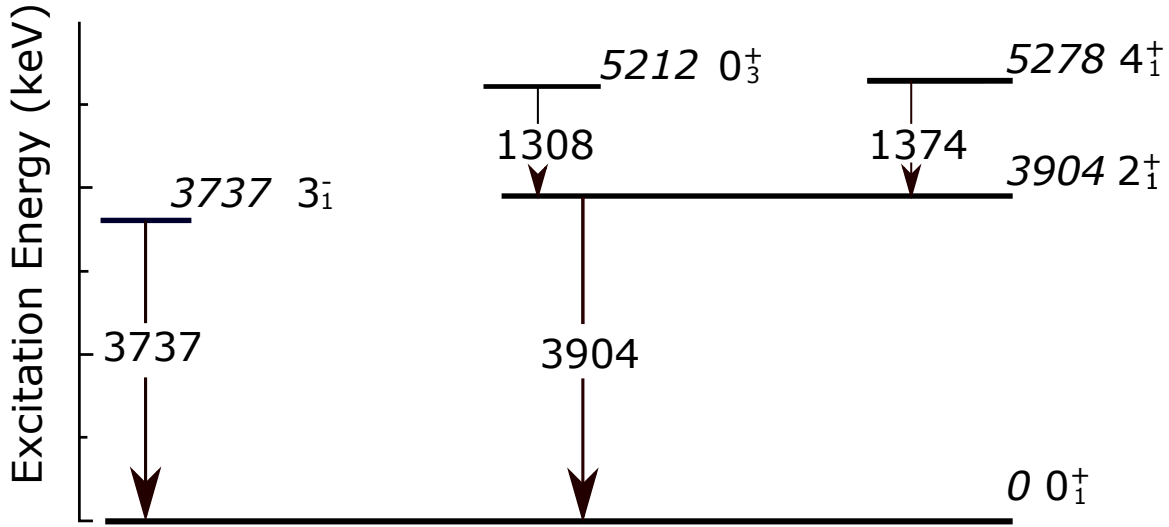
Figure 2.3: A simplified level scheme of ^{40}Ca. A level is shown only if at least one of its associated transitions were observed in the gamma-ray spectrum in this work. The data was extracted from Ref. [7].

2.4.1 Photoelectric Absorption

In photoelectric absorption, the full energy of the gamma ray is deposited into a single electron. The electron is ejected from its atom with kinetic energy equal to the energy of the gamma ray, E_γ, less the atomic binding energy E_b:

$$E_e = E_\gamma - E_b \ , \tag{2.12}$$

9
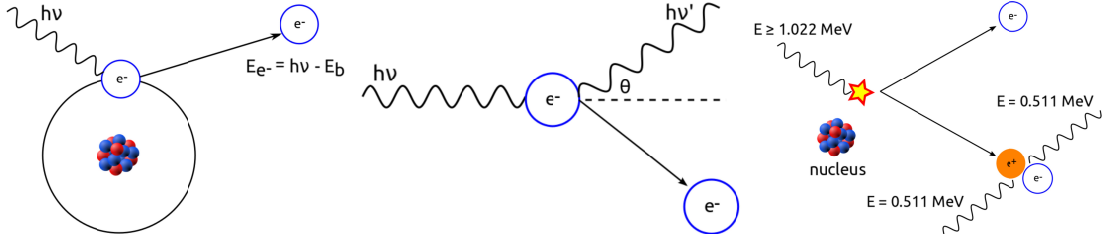
Figure 2.4: The three types of gamma-ray interaction with matter. The incident gamma ray has energy $E_\gamma = h\nu$, where h is the Plank's constant and ν is the frequency. In photoelectric absorption (left), the full energy of the gamma ray is absorbed by a single electron. In Compton scattering (centre), part of the gamma energy is absorbed by an electron while the rest of the energy is carried by another photon. In pair production (right), the gamma ray has $E_\gamma \geq 2m_ec^2 = 1.022$ MeV and produces a electron-positron pair. The Figure is reprinted from Ref. [19].

as illustrated in the left panel of Figure 2.4. For the gamma-ray transitions that are described in this thesis, $E \simeq E_\gamma$ because the E_b is on the order of eV to tens of eV while the energy of the gamma rays is on the order of MeV. If the interaction takes place in a semiconductor such as TIGRESS, the ejected electron deposits its full energy into nearby electrons to create electron-hole pairs. Photoelectric absorption in the detection medium therefore contributes to the full-energy photopeak in the detected gamma-ray spectrum, as illustrated in Figure 2.5.
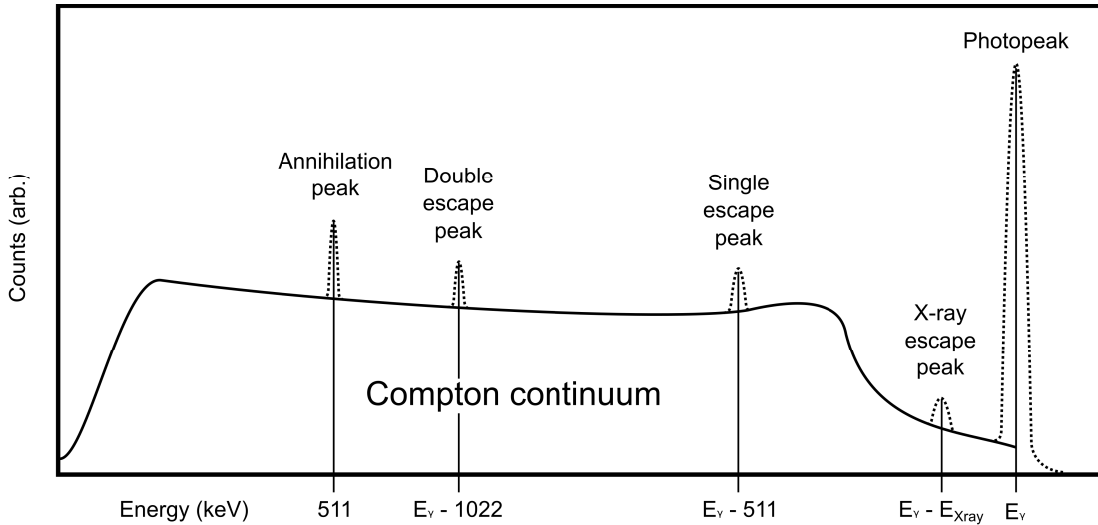
Figure 2.5: A generic gamma-ray spectrum for a mono-energetic gamma-ray source with $E_\gamma > 2m_ec^2 = 1.022$ MeV. The Figure is reprinted from Ref. [19].

2.4.2 Compton Scattering

The Compton continuum is a commonly observed background in gamma-ray spectra due to Compton scattering.. In Compton scattering, a part of the gamma-ray energy is deposited to an electron. The electron is ejected, similar to that in photoelectric absorption, while the rest of the incident gamma ray energy scatters away as another gamma ray, as illustrated in the centre panel of Figure 2.4. Partitioning of the energies between the electron and the scattered gamma ray depends on the scattering angle θ [20]:

$$E'_\gamma = \frac{E_\gamma}{1 + (E_\gamma/m_e c^2)(1 + \cos\theta)} \,, \tag{2.13}$$

$$E_e = E_\gamma - E'_\gamma \,, \tag{2.14}$$

where E_γ is the incident gamma-ray energy, E'_γ is the scattered gamma-ray energy, and E_e is the energy deposited into the electron with mass $m_e c^2 \simeq 511$ keV. If the scattered gamma-ray exits the detection medium without further interaction, the energy deposited into the detector would be E_e, which is lower than the incident E_γ. Compton scattering therefore contributes to the low-energy continuum in the detected gamma-ray spectrum, as illustrated in Figure 2.5.

2.4.3 Pair Production

The 511 keV peak is often observed in gamma-ray spectra of different sources due to pair production. Pair production may occur if the incident gamma-ray energy is greater than 1.022 MeV, which is twice the mass of an electron. In pair production the incident gamma ray produces a pair of electron and positron, each with mass $m_e c^2 = 511$ keV, as illustrated in the right panel of Figure 2.4. From the conservation of energy the electron-positron pair has total kinetic energy of $E_\gamma - 1.022$ MeV, which is deposited via excitation of the surrounding medium. The positron annihilates another electron as it slows down, and emits two 511 keV gamma rays back-to-back. If the pair production takes place outside of the detection medium, one of these two gamma rays may deposit its energy onto the detector. This contributes to the 511 keV annihilation peak in the detected gamma-ray spectrum, as illustrated in Figure 2.5. If the pair production takes place inside the detection medium and one of the annihilation (511 keV) gamma rays escapes the medium without further interaction, the total energy deposited in the medium is $E_\gamma - 511$ keV. Similarly if both annihilation gamma rays escape, the total energy deposition in medium is $E_\gamma - 2 \times 511$ keV $= E_\gamma - 1.022$ MeV. These two scenarios respectively contribute to the single and double escape peaks in the detected gamma-ray spectrum, as illustrated in Figure 2.5.

2.5 Doppler Shift Attenuation Method (DSAM)

The lifetimes that are discussed in this thesis are between the order of femtoseconds (fs) to picoseconds (ps). Measurements on such short time scales require special techniques such as the Doppler Shift Attenuation Method (DSAM). Following the theory of special relativity, the energy of a gamma ray that is emitted from a moving source is Doppler shifted. The Doppler-shifted energy that is observed in the LAB frame for a gamma ray with energy E_0 in the frame of the source depends on the speed of the source, v, and the angle between the directions of the source and the emitted gamma ray, θ:

$$E_\gamma = E_0 \frac{\sqrt{1-\beta^2}}{1-\beta \cos \theta} , \beta = v/c ,$$ (2.15)

where c is the speed of light.

Due to the conservation of momentum, the ^{40}Ca* that was described in Section 2.1 continues to travel in roughly the direction of the beam after its production in the carbon target. It then enters a gold stopper, as illustrated in Figure 2.6, where it slows down and eventually stops. The longer time the ^{40}Ca travels in the gold backing, the slower it gets. As a result, gamma rays emitted at different times experience different amounts of Doppler shift, and the line shape of the gamma-ray spectrum contains information of the lifetime of the excited state, which can then be extracted in offline analyses. This technique is called the Doppler-shift attenuation method (DSAM) [21]. The lifetimes in this thesis
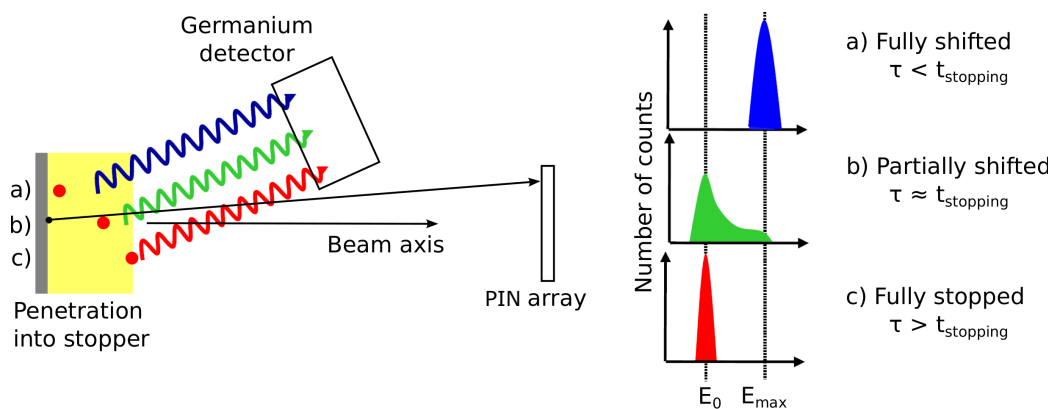
Figure 2.6: The excited ^{40}Ca is produced in the carbon target (grey) and enters the gold backing (yellow). The energy of the gamma ray is Doppler shifted, which depends on the lifetime, τ, of the excited state. The Figure is reprinted from Chrystian Droste, via private communication with Kris Starosta.

were extracted, while accounting for the stopping process and the gamma-ray spectra's dependence on detector geometry, using Geant4, a framework for Monte-Carlo simulations. The simulations are discussed in detail in Chapter 5.

2.6 The Time-Coincidence Method

In a multi-detector system, timing can be used to correlate events in separate detectors to the same physical process. If a fast process is known to emit more than 1 radiation, such as an alpha particle and a gamma ray, the time-coincidence method [22] can be used to correlates these events and reduce background. Figure 2.7 shows an example system of two detectors being *in-coincidence*. If the two detectors each register a signal within a time
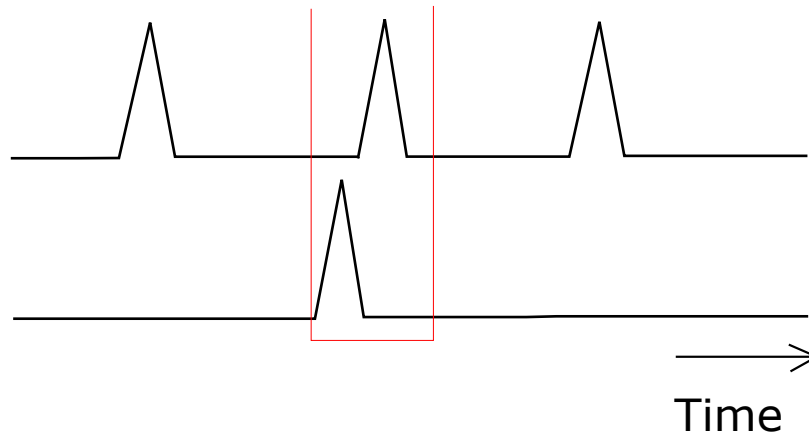
Figure 2.7: A illustration of two detectors with signals *in-coincidence*, within the red window, with one another.

window, the signals are *in-coincidence*, and the signals are kept. On contrast, Figure 2.8 shows the signals in the detectors *out-of-coincidence*. The *out-of-coincidence* signals are
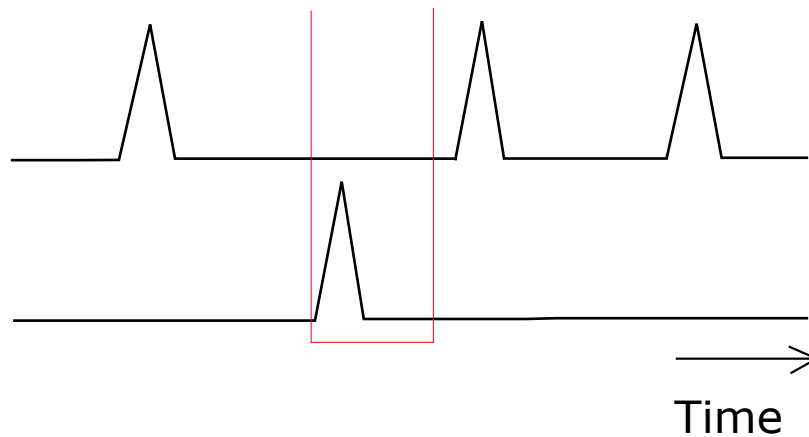
Figure 2.8: A illustration of two detectors with no signals *in-coincidence* within the red window. These signals are considered *out-of-coincidence*.

excluded from further analysis.

The time-coincidence method reduces random background because it is less probable for both detectors to register random background in the same coincidence window. If the probability of one detector registering a random background in the window is 0.01, the

probability of both detectors registering signals from random background is $0.01^2 = 0.0001$. Although not all background can be eliminated, it can be significantly reduced.

Chapter 3

Experiment

The experiment described in this thesis was performed in ISAC-II [23] at TRIUMF [24]. The beam was accelerated using the superconducting LINAC and delivered to the TIGRESS station in the experimental hall. Figure 3.1 shows a schematic drawing of the ISAC halls with locations of these devices.
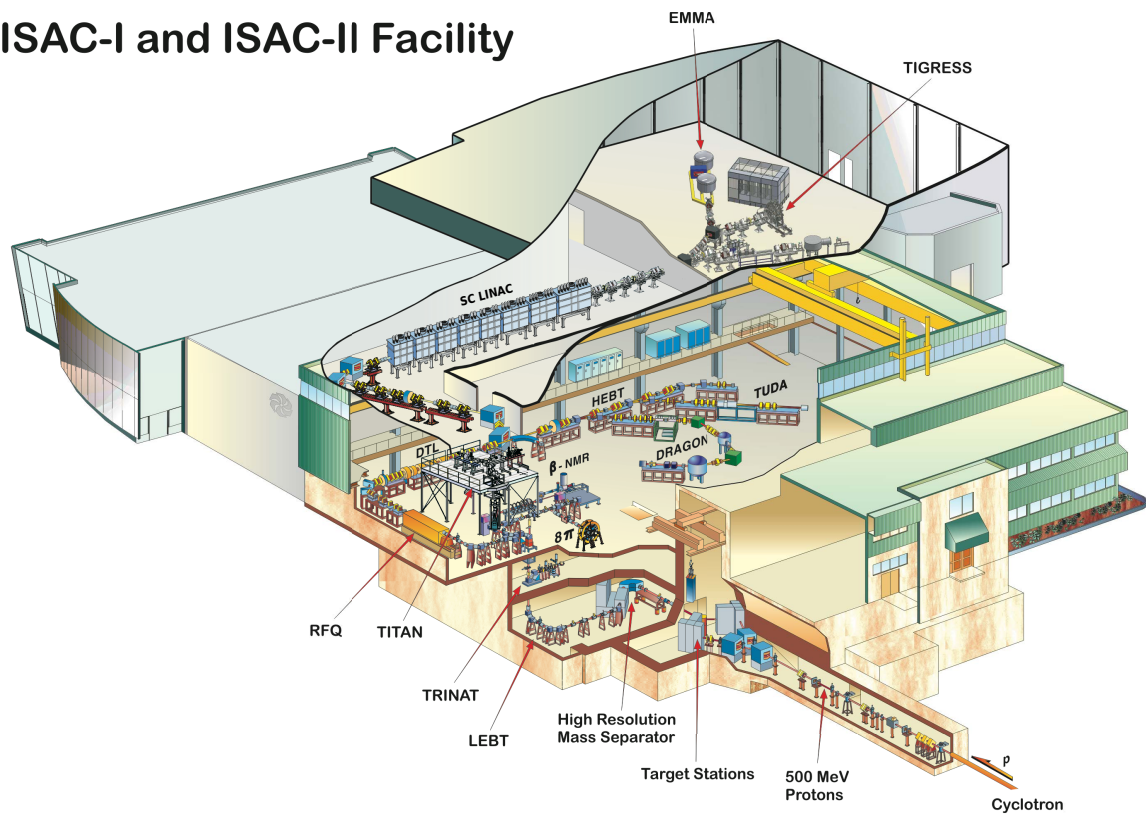
Figure 3.1: Schematic drawing of the TRIUMF ISAC experimental halls. The experiment described in this thesis was performed using the superconducting LINAC (SC LINAC) and TIGRESS in ISAC-II. The figure is reprinted from Ref. [25].

3.1 The Beam and the Superconducting RF LINAC

The beam was supplied from a cylinder of isotopically pure ^{36}Ar. It was then charge-bred (ionized) with the Off-Line Ion Source (OLIS), as described in detail in Ref. [26], and accelerated in stages with the Radio-Frequency Quadrupole (RFQ) and the drift tube LINAC (DTL). Finally, it was accelerated using the ISAC II superconducting RF LINAC to 63 MeV and electromagnetically steered to the TIGRESS experimental station.

The beam was delivered in bunches, as a result of the oscillation of the RF voltage in the cavities of the LINAC. Only particles injected into the cavity in-phase with the RF were accelerated and as a result, the accelerated beam was in bunches that had the same frequency as the RF. This RF signal, which correlated to the beam bunches, can be used as a reference to establish timing of the detectors. Timing of the detectors is described in Section 4.1.2 of this thesis.

3.2 The TIGRESS HPGe Array

Gamma rays in this experiment were detected using the TRIUMF-ISAC Gamma Ray Suppressed Spectrometer (TIGRESS). TIGRESS is 16-clover array of segmented high-purity germanium (HPGe) detectors. Each detector is made of 4 HPGe crystals. The low band gap of HPGe allows for fine energy resolution, while having multiple crystals in a single detector allows for finer angular resolution in addition to energy add-back. The energy add-back decreases the Compton background while improving the efficiency of the overall detector. Add-back is described in Section 3.2.3. Figure 3.2 shows a front-view of seven TIGRESS detectors. The HPGe crystals in TIGRESS were cooled to liquid nitrogen temperature during operation. Background suppression of Compton scattering, described in section 3.2.2, was enabled by the bismuth germanium oxide (BGO) shields.
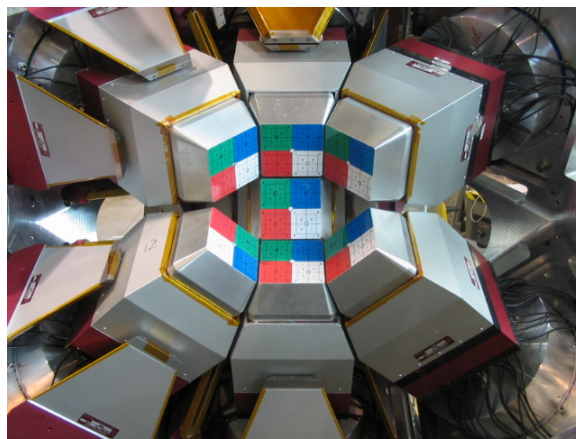
Figure 3.2: Front view of seven TIGRESS detectors. Each color on a detector correspond to a separate HPGe crystal. The red-and-silver plates are BGO shields used for Compton suppression. The photograph is reprinted from Ref. [27].

3.2.1 Angular Groups of TIGRESS

The 16 detectors are arranged in rings of constant polar angles with respect to the beam axis. The forward, centre, and backward positions have polar angles 45°, 90°, and 135° respectively. Grouping TIGRESS in pairs of two crystals further divides the pairs into six rings, centred at 35°, 55°, 80°, 100°, 125° and 145°.

3.2.2 Compton Suppression

If left untreated, partial gamma-ray energy deposits, or Compton scattering which is described in Section 2.4.2, in the TIGRESS detectors could create lower-energy continua that significantly contribute to the background in the gamma-ray spectra. These events could be suppressed by applying an anti-coincidence logic between the HPGe crystals and the BGO shields that surrounded them. A TIGRESS event could be dropped from the data stream if the HPGe crystal and its corresponding BGOs both registered energy deposits in a (145 ns) time-coincidence window. Timing of the detectors is described in Section 4.1.2.

3.2.3 Gamma-Ray Energy Add-back

In a single TIGRESS detector, if an incident gamma ray partially deposits its energy in one crystal and scatters into the other crystal(s), the full energy of the gamma ray could be reconstructed by adding the energy of the neighbouring crystals. This reconstruction is referred to "add-back", following the nomenclature in Ref. [28]. By re-combining the multiple partial energy deposits that originated from a single gamma ray, the Compton background can be reduced while improving the efficiency of the full TIGRESS detector. The full energy of the incident gamma ray can be added-back if adjacent crystals in the same TIGRESS detector record energy deposits in a time-coincidence window. Section 4.1.2 describes the timing in detail.

3.3 The TIGRESS Integrated Plunger

The TIGRESS Integrated Plunger (TIP) is a configurable tool that is used in conjunction with TIGRESS for Doppler-shift lifetime studies. Ref [29] describes TIP in detail. In this thesis TIP was configured with a DSAM target and the PIN Array. Figure 3.3 shows TIP inside TIGRESS.

3.3.1 PIN Array

The PIN Array was housed inside the TIP chamber and used for charged-particle detection. It is composed of 44 silicon PIN diodes with their centres arranged in four rings of similar polar angles with respect to the beam axis. Figure 3.4 shows the PIN Array inside the TIP chamber.
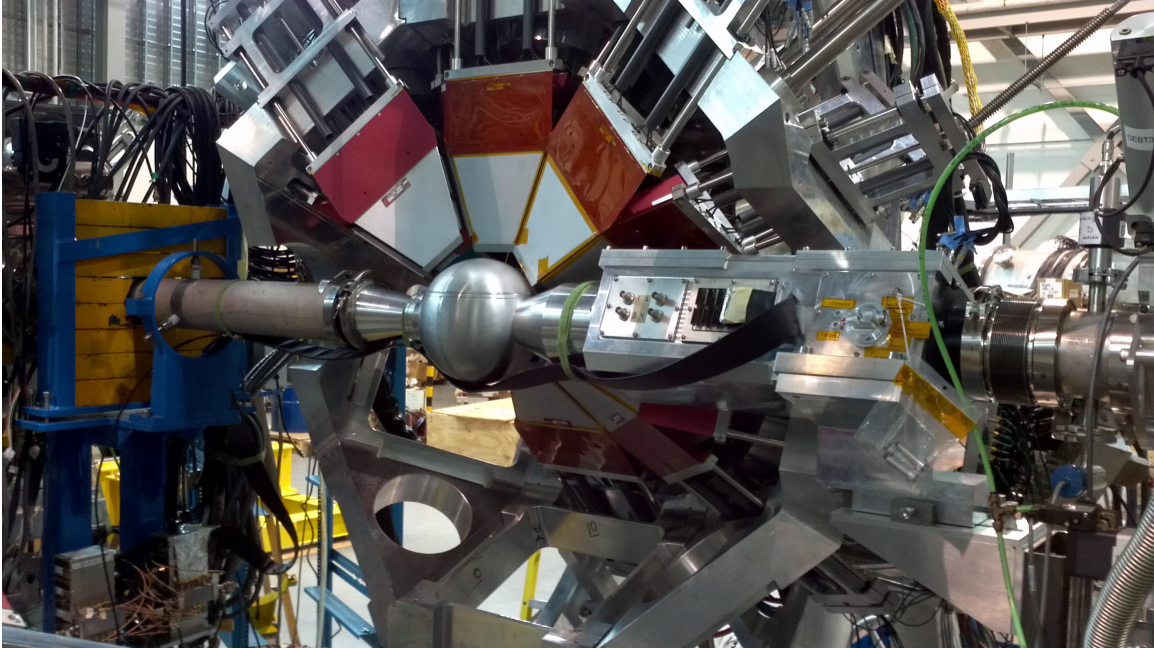
Figure 3.3: The TIGRESS Integrated Plunger (TIP) mounted inside TIGRESS. The photograph was reprinted from Ref. [29].
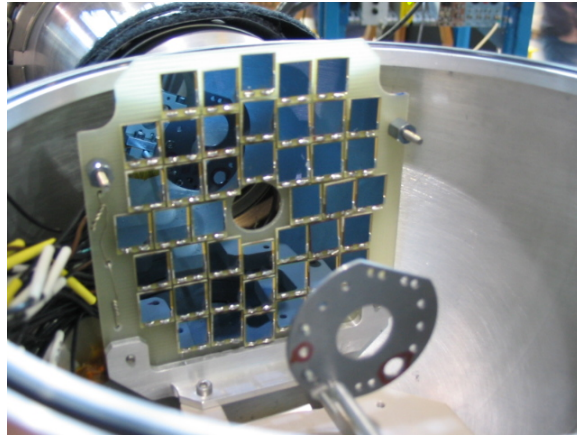
Figure 3.4: The PIN Array and target wheel inside the TIP chamber. The photograph was reprinted from private communication with Phil Voss.

In this experiment the PIN Array was placed 63.9 mm downstream of the target wheel. Each PIN diode was reverse-biased [30] to increase its depletion zone that was sensitive to particle detection. Dimensions and a list of positions of the PIN diodes on the PIN Array can be found in Ref. [29].

The waveform of the PIN diodes also provided a means of particle identification, described in detail in Ref. [30], which could be used to provide additional sensitivity to reaction channels.

3.3.2 The Target

The experiment used a single target with $^{\text{nat.}}$C, natural-abundance carbon which is 98.9% ^{12}C, on gold backing. The target was made via physical vapor deposition of a gold layer onto a commercially available carbon foil with a thermal evaporation source. The gold layer was thick enough to fully stop all ^{36}Ar beams and the product ^{40}Ca's. The carbon layer was 0.43 mg/cm^2 (1.9 μm) and the gold layer was determined to be 22.8 mg/cm^2 (11.8 μm). Figure 3.5 shows a photograph of the target after the experiment. Details of the target

Figure 3.5: Photograph of the target mounted on the left position of the target wheel, taken after the experiment. Mounted on the right position of the target wheel was a fluorescent screen for visual checks of the beam profile. The photograph was reprinted from private communication with Phil Voss.

can be found in Ref. [31]. Further discussion on the backing thickness can be found in Section 5.1.

3.4 Reaction Channels

The combination of the ^{36}Ar beam on the $^{\text{nat.}}$C target with gold backing allowed for a wide assortment of reaction channels. In addition to Rutherford scattering of the beam and target nuclei, and the Coulomb excitation of the gold backing, the following reactions were also observed:

1. Coulomb excitation of ^{36}Ar ,

2. ^{36}Ar + ^{12}C $\longrightarrow$ ^{37}Ar + ^{11}C ,

3. ^{36}Ar + ^{12}C $\longrightarrow$ ^{44}Ti + α ,

4. ^{36}Ar + ^{12}C $\longrightarrow$ ^{40}Ca + 2α .

Presence of the products in these reaction channels were verified with gamma-ray spectroscopy, which is described in more detail in Chapter 4.

3.5 The Data Acquisition System

TIGRESS and the PIN Array occupied different channels of the same TIGRESS data acquisition system (DAQ). It was a fast digital DAQ custom-designed for TIGRESS, described in detail in Ref. [32]. The DAQ provided triggering logic, digitized the signals with real-time pulse heights and timing, and stored the digitized waveforms. These waveforms were used to fit for more precise amplitude and rise time for particle identification in offline analyses.

3.5.1 TIGRESS DAQ Architecture

Figure 3.6 shows a schematic drawing of the TIGRESS DAQ architecture. The TIGRESS DAQ contained two types of custom-made electronic cards, the TIG-10 and the TIG-C [32]. Each TIG-10 card contained 10 front end (FE) modules and one sub-event collector (COL-Channel). Each TIG-C card could be configured as either a primary collector (COL-Master) or a secondary collector (COL-Slave) node. Different configurations of the TIG-C cards were achieved with different firmwares.

Signals from the detectors were first collected in the front end modules where they were digitized and processed. Information from the front ends was then sent to the Collector (COL) nodes where they were concentrated and built into sub-events according to the trigger conditions set by the experimenter. The trigger logic was determined at the secondary collectors and then the primary collector [32]. If a signal was accepted by the primary collector, a time stamp of this primary trigger was recorded using a 100 MHz ADC clock, and instructions were sent to the secondary collectors to record the waveforms and the hit information to the DAQ computer through the VME interface.

3.5.2 The MIDAS Interface

The TIGRESS DAQ was controlled through the Maximum Integrated Data Acquisition System (MIDAS) interface [33,34]. The interface allowed the experimenter to pass electronics parameters and triggering conditions to the DAQ, and stored the data read out from the VME modules in the MIDAS file on the hard drive. The MIDAS file format stored the output from DAQ channels, such as time and trigger number, in a collection of event fragments that were not time-ordered. The hit information and waveforms stored in the MIDAS files can be extracted for offline analyses. The data sorting procedure is explained in Section 4.1.
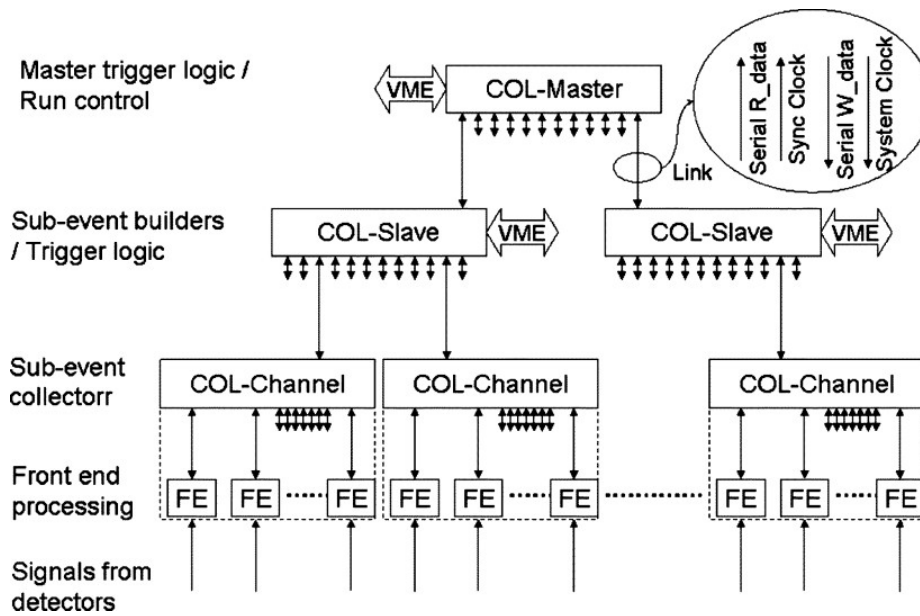
Figure 3.6: Block diagram of the TIGRESS DAQ architecture. The primary collector (COL-Master) and secondary collectors (COL-Slave) were TIG-C cards with different firmware and COL-Channels and front ends (FE) were components of the TIG-10 cards. The figure is reprinted from Ref. [32].

Chapter 4

Analysis of Experimental Data

4.1 Data Sorting Procedures

4.1.1 MIDAS to SFU

The data was initially saved from the TIGRESS DAQ in the MIDAS file format as described in Section 3.5.2. It was then converted offline into the SFU format, described in this Section, to correlate DAQ fragments to physical events for further analysis. The event fragments that were recorded by the DAQ were assembled by trigger number, and fragments with the same trigger number were reconstructed into an event in the SFU format. This means that a single SFU event may contain hit information from multiple DAQ channels corresponding to multiple detector systems. In the reconstruction process, the DAQ channels were mapped into position IDs of the different detector systems. Waveforms of the PIN diodes were also fitted for rise times which could then be used for identifying the type of radiation that hit the PIN diode. Section 4.3 discusses the algorithm for particle identification with waveforms in more detail. The sorted events in the SFU format were written into a file, which is referred to as an SFU file in this thesis.

4.1.2 Timing of the Detectors

The time assigned to a hit on a detector was derived from a combination of three parameters: the time stamp, the LINAC RF, and the constant fraction discrimination (CFD). The time stamp was assigned to the event from its primary trigger using the 100 MHz ADC clock, as described in Section 3.5.1. It is chronological and unique to each event. The CFD is derived from the online signal processing of the TIGRESS FE, as described in Ref. [32]. The sampling period for the CFD is 1/16 of the ADC clock, which enabled the CFD to provide finer correction to the time stamp. The RF signal, as described in Section 3.1, came directly from the LINAC and served as an external time reference for each beam bunch. Subtracting the RF time from the CFD-corrected time correlates the hits from different detector systems to the beam bunch.

4.1.3 Time Coincidence

Time coincidence between TIGRESS and the PIN Array was enforced to correlate PIN and TIGRESS readouts and to suppress random gamma rays in the background. Because the trigger window of the DAQ was on the order of μs while the timing difference between the TIGRESS and PIN Array hits that came from a single reaction was on the order of 100 ns, not all hits that were accepted into a single DAQ event came from the same reaction. Figure 4.1 shows the timing correlation between TIGRESS and PIN Array for the events recorded by the DAQ. To remove the random background, the timing differences between TIGRESS and PIN Array hits were calculated on an event-by-event basis.

Figure 4.1: The 2D histogram of the timing correlation between TIGRESS and PIN Array, with reference to RF before enforcing time coincidence.

Due to the electronics in the experimental setup, a TIGRESS hit lags a PIN Array hit by approximately 3500 ns on average even when the gamma ray and charged particle originated from the same reaction. As a result the following algorithm was used to enforce time coincidence for hits in a single SFU event:

1. Check the time for all TIGRESS hits. The time of the last TIGRESS hit was stored as t_{max}.

2. Check the time for all PIN hits. The time of the first PIN hit was stored as t_{min}.

3. For a TIGRESS hit at time t_{TIG}, calculate $t_{\mathrm{diff}} = t_{\mathrm{TIG}} - t_{\mathrm{min}}$. Keep this hit if its t_{diff} is within a prescribed range.

23

4. For a PIN hit at time t_{PIN}, calculate $t_{\text{diff}} = t_{\text{max}} - t_{\text{PIN}}$. Keep this hit if its t_{diff} is within the same prescribed range as (3).

A diagram illustrating the calculation of the time difference, t_{diff}, that was used for the acceptance logic is shown in Figure 4.2. In each SFU event, hits with t_{diff} within the 100 ns

In a raw event recorded by the DAQ:

🅸 i^{th} TIGRESS hit   Save this hit?
ⓘ i^{th} PIN hit
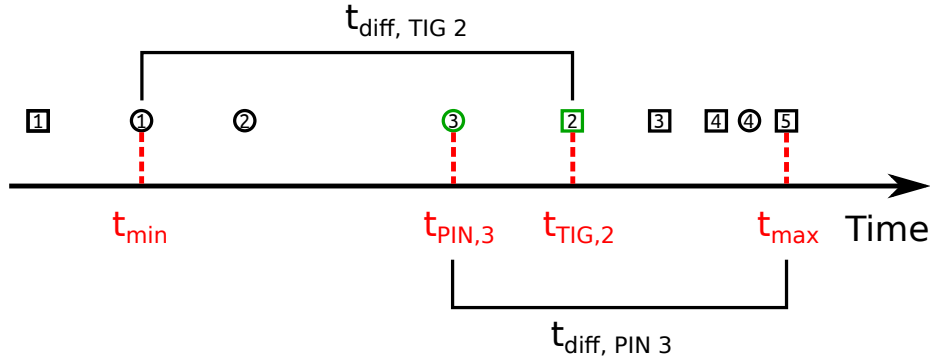
Figure 4.2: An illustration of the time difference calculation that was used to determine whether an event (green) satisfied TIGRESS-PIN time coincidence.

window, from 3450 ns to 3550 ns, were considered to satisfy TIGRESS-PIN time coincidence. Hits that did not satisfy time coincidence were dropped from the SFU event. The events were then written into a second, time-correlated, SFU file. Figure 4.3 shows the TIGRESS-PIN time correlation after enforcing timing coincidence.

In Figure 4.3, a small fraction ($<0.02\%$) of the points are above the diagonal and outside of the cut. These events were accepted by the algorithm that was described earlier in this section because the TIGRESS signals were selected to be in time-coincidence with the earliest PIN signal in each SFU event. When there were multiple PIN signals in an SFU event, there is a chance that $t_{\text{TIG}} - t_{\text{PIN}}$ fell below the minimum t_{diff} if some PIN signals have times significantly later than others. Treatment of this type of false coincidence will be discussed in Section 4.1.5.

4.1.4 Reaction Channel Selection for ^{40}Ca

Additional sensitivity to the ^{40}Ca reaction channel can be achieved by selecting the fold, the number of hits in separate PIN diodes, in the PIN Array. Among all the reaction channels that were described in Section 3.4, only the one which produces ^{40}Ca,

$$^{36}\text{Ar} + {}^{12}\text{C} \longrightarrow {}^{40}\text{Ca} + 2\alpha \ , \tag{4.1}$$

24
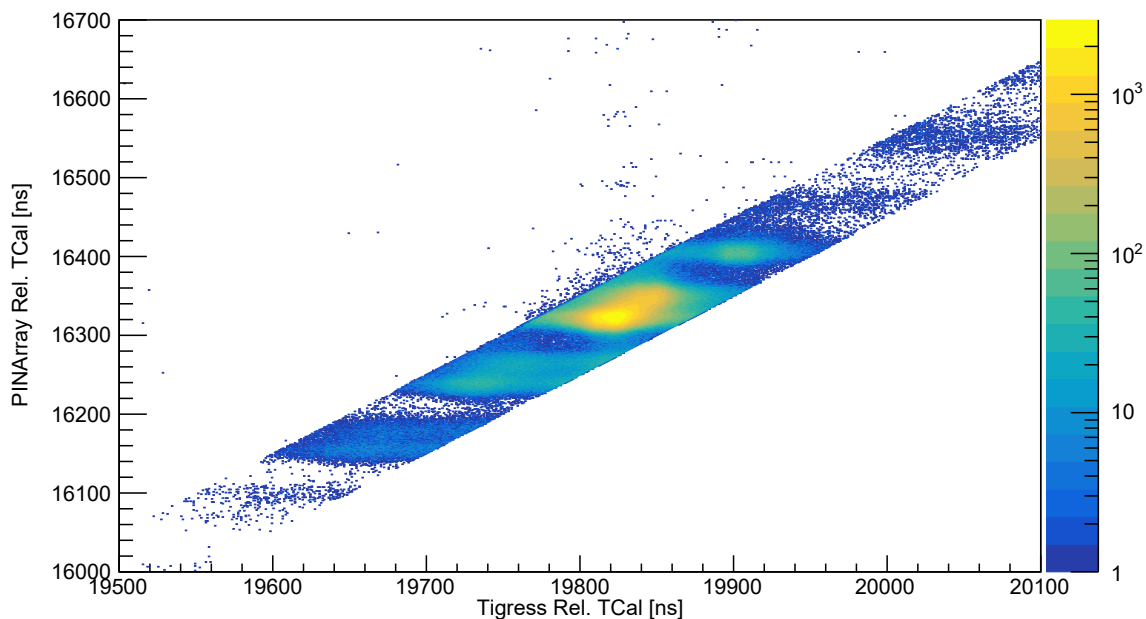
Figure 4.3: The 2D histogram of the timing correlation between TIGRESS and PIN Array, with reference to RF after enforcing time coincidence.

emits two alpha particles. Consequently the time-coincident data was further sorted, where events in the SFU format with PIN Array fold 2 were written to a third SFU file.

4.1.5   Final Timing Analysis for the Coincidence Method

The algorithm that was described in Section 4.1.3 focused on the time coincidence between TIGRESS and PIN Array. However, two PIN Array signals that were in coincidence with TIGRESS might not necessarily come from the same reaction. The left panel of Figure 4.4 shows the symmetrized time correlation between the two PIN signals sorted from the TIGRESS-PIN time coincident, PIN Array fold 2 events as described in Section 4.1.4. The four bright spots correspond to time-coincident PIN signals in each beam bunch. The sprinkled points outside of the bright spots are results of two PIN signals in an SFU event that were in coincidence with TIGRESS but not with one another. These points were eliminated by excluding the SFU events that had time differences between the 2 PIN signals greater than 40 ns. The PIN-PIN time correlation plot with these events excluded is shown in the right panel of Figure 4.4. Finally, TIGRESS-PIN time coincidence was enforced again on the PIN-PIN coincident events, using the same time window as in Section 4.1.3. Instead of calculating t_{diff} from the earliest PIN signal, this time t_{diff} was calculated with respect to the mean time between the two PIN signals. TIGRESS signals that were not in coincidence with the mean time of the two PIN signals were excluded from the analysis. SFU events that
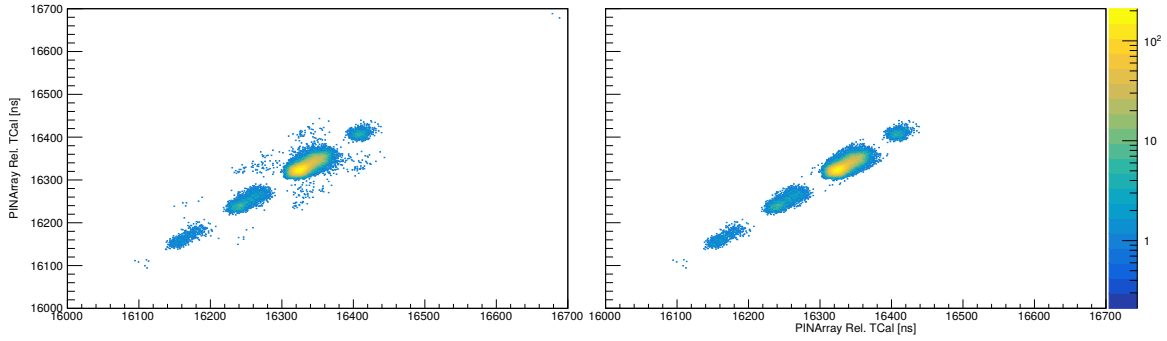
Figure 4.4: The symmetrized 2D histograms of the timing correlation between the two signals in the PIN Array, sorted from the PIN Array fold 2 events before (left) and after (right) enforcing PIN-PIN time coincidence. The times are with reference to RF.

satisfied the conditions described in this section were written to a fourth SFU file. This SFU file was used as the basis for the rest of the analysis. Figure 4.5 shows the TIGRESS-PIN time correlation sorted from these SFU events. The sprinkled, falsely-coincident points in Figure 4.3 are no longer present.

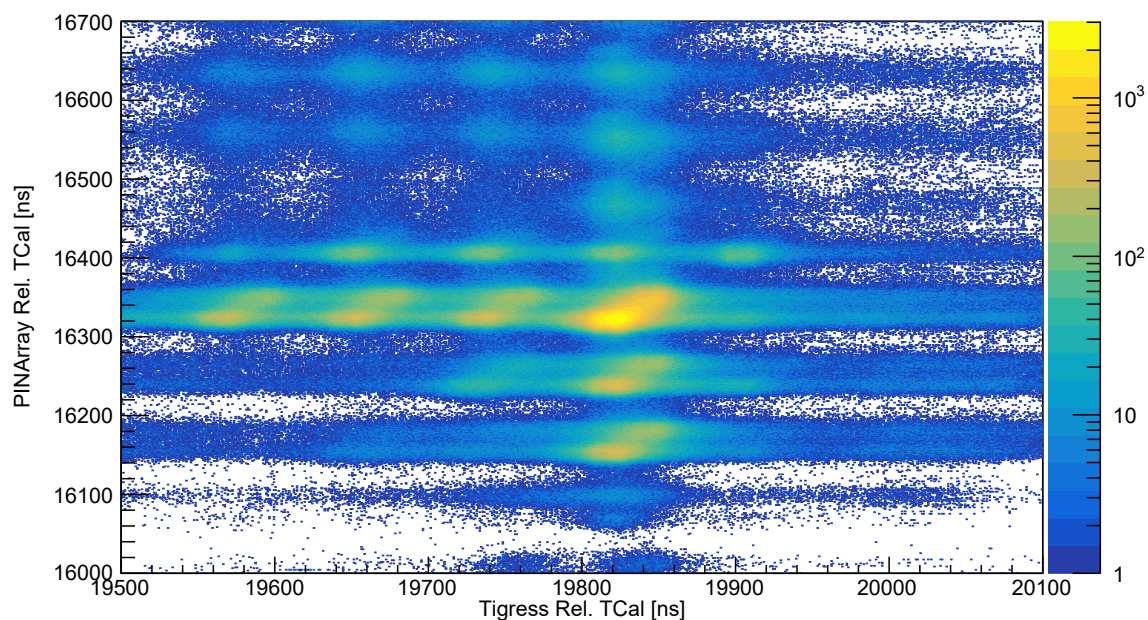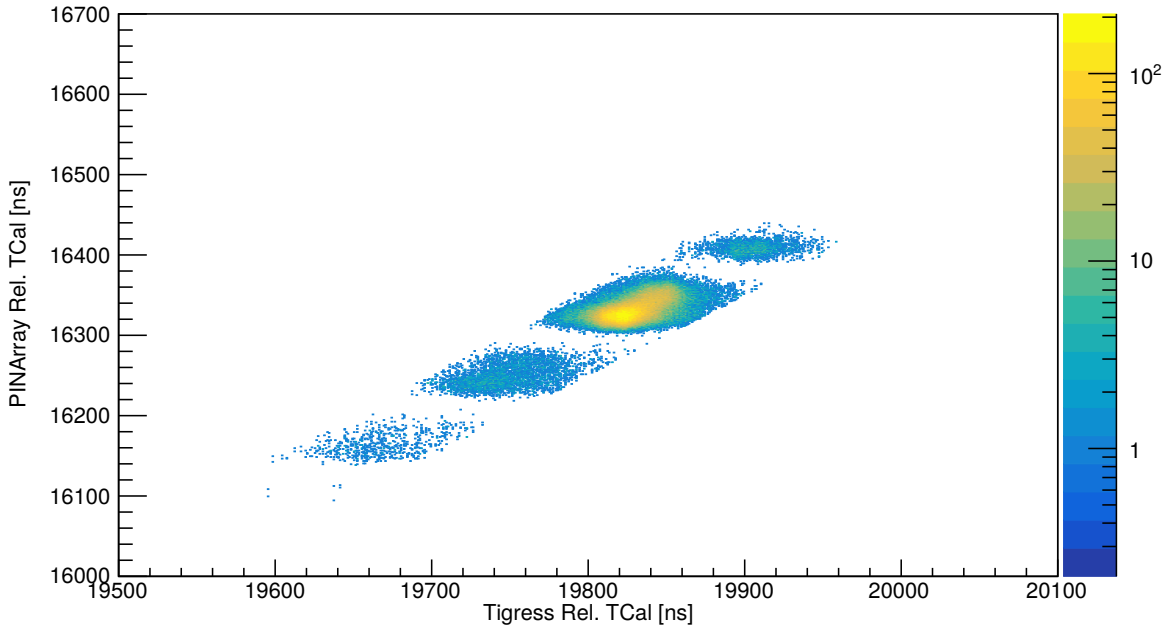Figure 4.5: The 2D histogram of the timing correlation between TIGRESS and PIN Array, with reference to RF after PIN-PIN time coincidence and TIGRESS-PIN coincidence from the mean PIN time.

4.1.6 Doppler-shift Grouping

Gamma rays that were emitted at nearly 4π solid angle from the target could be detected thanks to the nearly spherical coverage of the TIGRESS array. This meant that different

amounts of Doppler shift could be observed for gamma rays that were emitted from moving nuclei. The gamma-ray energy that was measured by the TIGRESS crystal, E_γ, is related to the energy of the gamma ray in the frame of the parent nucleus, E_0, as

$$E_\gamma = \frac{\sqrt{1-\beta^2}}{1-\beta\cos\theta}E_0 \ , \tag{4.2}$$

where β is the ratio between the speed of the nucleus and the speed of light, and θ is the angle between the directional vectors of the nucleus and the gamma ray. For simplicity, a quantity that is called the Doppler-shift factor was defined,

$$D = \frac{\sqrt{1-\beta^2}}{1-\beta\cos\theta} \ . \tag{4.3}$$

With this Doppler-shift factor, Equation 4.2 becomes

$$E_\gamma = DE_0 \ . \tag{4.4}$$

The Doppler-shift factor was calculated on an event-by-event basis by reconstructing the events using momentum conservation from the detected momenta of the alpha particles, the spatial position of the TIGRESS crystal, and the momentum of the beam. In the entrance channel of the reaction, it was assumed that the ^{36}Ar reacted at the full beam energy of 63 MeV on the face of the target and the ^{12}C was stationary. The momentum of the ^{40}Ca can then be fully determined using

$$\vec{p}_{\text{Ca}} = \vec{p}_{\text{beam}} - \vec{p}_{\alpha 1} - \vec{p}_{\alpha 2} \ , \tag{4.5}$$

where $\vec{p}_{\text{beam}}$ is the momentum of the beam, which was calculated from the beam energy and the mass of ^{36}Ar, and $\vec{p}_{\alpha 1}$ and $\vec{p}_{\alpha 2}$ were determined from the energies deposited and spatial positions of the PIN diodes in the PIN Array. The direction of each alpha particle was assumed to be that from the centre of the target to the centre of the PIN diode on which the alpha particle deposited its energy. Energy calibration of the PIN Array is discussed in Section 4.2.3. The energies of the alpha particles were then corrected for stopping in the target and backing using TRIM simulations [35]. Using Equation 4.5 with these assumptions and the known mass of ^{40}Ca, β in Eq. 4.4 was calculated. The $\cos\theta$ in Eq. 4.4 was also fully determined,

$$\cos\theta = \hat{e}_{\text{Ca}} \cdot \hat{e}_\gamma \ , \tag{4.6}$$

where $\hat{e}_{\text{Ca}}$ is the unit vector in the direction of $\vec{p}_{\text{Ca}}$ from Equation 4.5, and $\hat{e}_\gamma$ is the unit vector pointing from the centre of the target to the centre of the TIGRESS crystal that

detected the gamma ray. The histogram of experimentally-determined Doppler-shift factors is shown in Figure 4.6.
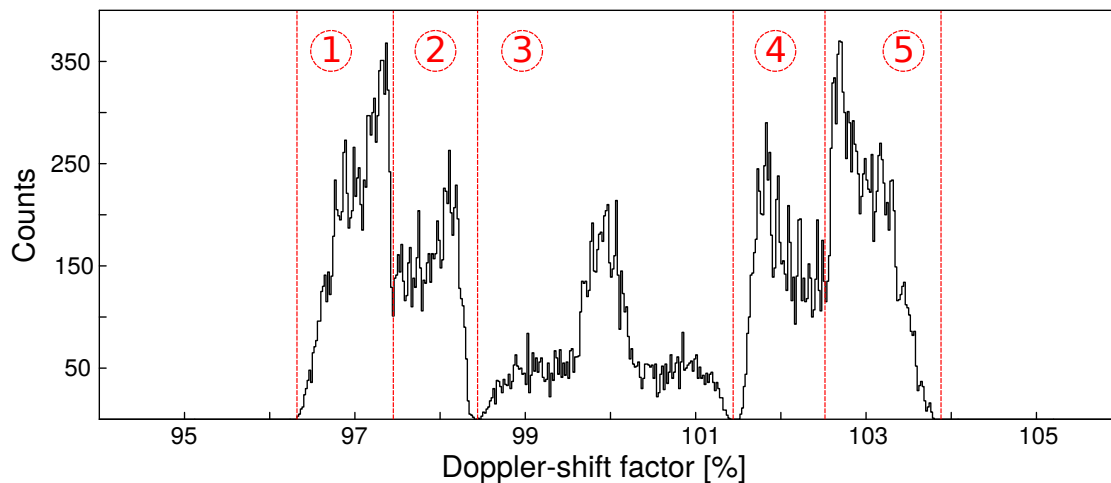
Figure 4.6: Histogram of experimentally-determined Doppler-shift factors reconstructed from time-coincident data with PIN Array fold 2. Regions between dotted red lines are defined as Doppler-shift groups, with the Doppler-shift group number in the circle.

Gamma rays were sorted into groups with similar Doppler-shift factors to improve the sensitivity of Doppler-shift lifetime measurement. The boundaries of the Doppler-shift groups were empirically defined at the natural boundaries in the Doppler-shift factor histogram. These boundaries are depicted as dotted red lines in Figure 4.6.

4.2 Detector Calibrations

4.2.1 TIGRESS Energy Calibration

Energy calibration of the TIGRESS crystals was performed with three standard sources: ^{152}Eu, ^{56}Co, and ^{133}Ba. This energy calibration was then cross-checked near the 2^+ peak of ^{40}Ca using the 3^-_1 to 0^+ transition in ^{40}Ca at 3737 keV. The lifetime of the 3^- state is approximately 60 ps which is 2 orders of magnitude longer than the time that was required for the ^{40}Ca to fully stop in the gold backing. As a result, no Doppler shift was expected for this peak. Figure 4.7 shows the TIGRESS spectra in this energy range, taken during the production runs. The 3737 keV peaks aligned across crystals at the energy that was consistent with literature values. The y-axis in Figure 4.7 was defined as

$$\text{Crystal} = (pos - 1) \times 4 + col \ , \tag{4.7}$$
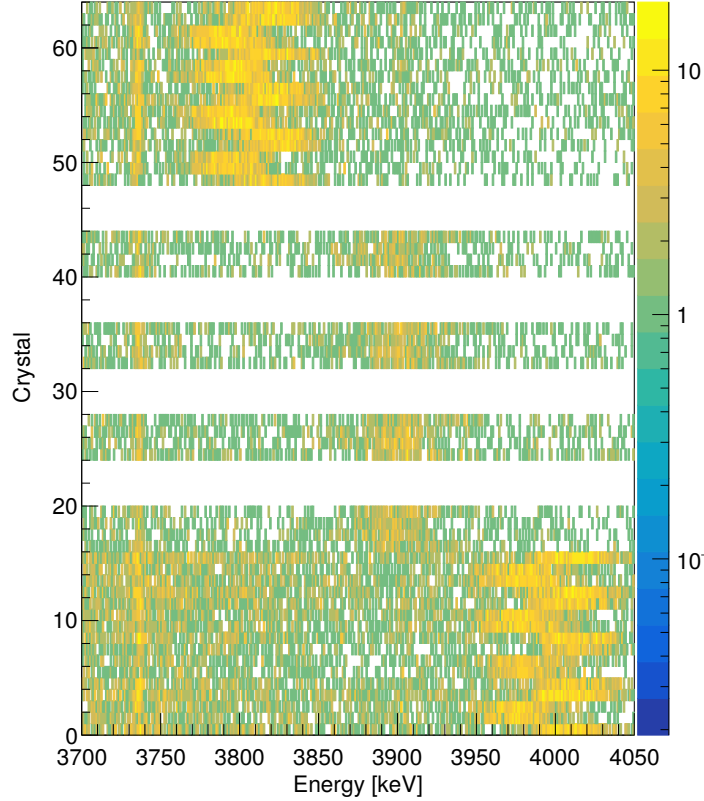
Figure 4.7: The calibrated energy spectra of TIGRESS near the 2^+ peak. The fully stopped peak at 3737 keV is the 3^- to 0^+ transition. The Doppler-shifted peak is the 2^+ to 0^+ transition. The 4 empty horizontal lines belonged to the TIGRESS positions that were not used in this experiment.

where *pos*, ranges from 1 to 16, is the detector number and *col*, ranges from 0 to 3, is the crystal number in each detector. For example, crystal 0 of detector 5 would have a y-value of $(5-1) \times 4 + 0 = 16$.

4.2.2 TIGRESS Relative Efficiency Calibration

Because the HPGe detection efficiency is energy dependent, relative efficiency calibration is needed to compare the intensities of gamma-ray peaks at different energies. To enable the intensity comparison between the 1374 keV transition from 4^+ to 2^+ and the 3904 keV transition from 2^+ to 0^+ in ^{40}Ca, a relative efficiency calibration was performed for the TIGRESS array using a ^{56}Co source. The relative efficiencies for 10 ^{56}Co peaks between 1038 keV and 3548 keV, with energies E_i, were calculated:

$$\epsilon_i = A_i/I_i \ , \tag{4.8}$$

where A_i is the area of the peak and I_i is the probability of emitting the gamma ray. Normalization was not necessary because the constants cancel while calculating the ratio between efficiencies at two different energies. Then, a quadratic function was fitted to the natural log of the efficiency vs. the natural log of the energy in keV, as described in Ref. [36]. Figure 4.8 shows these natural logs with the best fit and the 90% confidence interval. From
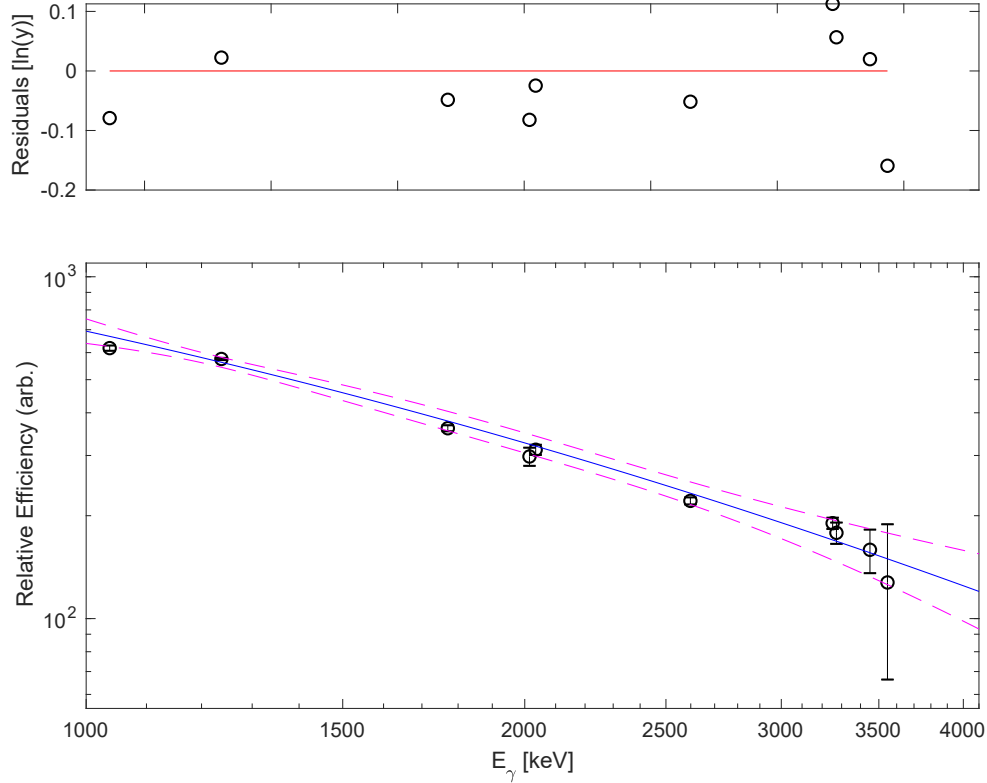
Figure 4.8: TIGRESS relative efficiency plotted as a function of gamma-ray energy in keV. The data points were calculated following Eq. 4.8. The dominant uncertainty in the error bars came from the uncertainty in counts. The best-fit is shown as the blue curve, and the 90% confidence band is illustrated by the dashed magenta lines.

this fit, the ratio between the TIGRESS efficiencies at the ^{40}Ca 4^+ peak and its 2^+ peak was determined to be $4(\pm1):1$. The $\sim 25\%$ uncertainty is a result of the low counts in the high-energy ^{56}Co peaks, and the confidence band quickly diverges beyond the range of well-known data points. The result is consistent with the rough estimates given by the GRIFFIN online efficiency calculator [37]. The uncertainty in energy as a result of Doppler shift is much smaller than the uncertainty from the fit, and it disappears when the uncertainties are added in quadrature. To be conservative, the analysis in this thesis takes the lower bound of the ratio and will treat the efficiency ratio as $3:1$.

4.2.3   PIN Array Energy Calibration

Energy calibration of the PIN Array was performed for each PIN diode using the triple-alpha source, which was composed of ^{239}Pu, ^{241}Am, and ^{244}Cm. The highest energy in the triple-alpha source was 5.8 MeV. The energy calibration was then cross-checked in the higher-energy range with the Rutherford scattering data from the production runs. Figure 4.9 shows the comparison between spectra for the inner-most ring of PIN Array from the experiment and GEANT4 simulation which is described in Section 5.1.
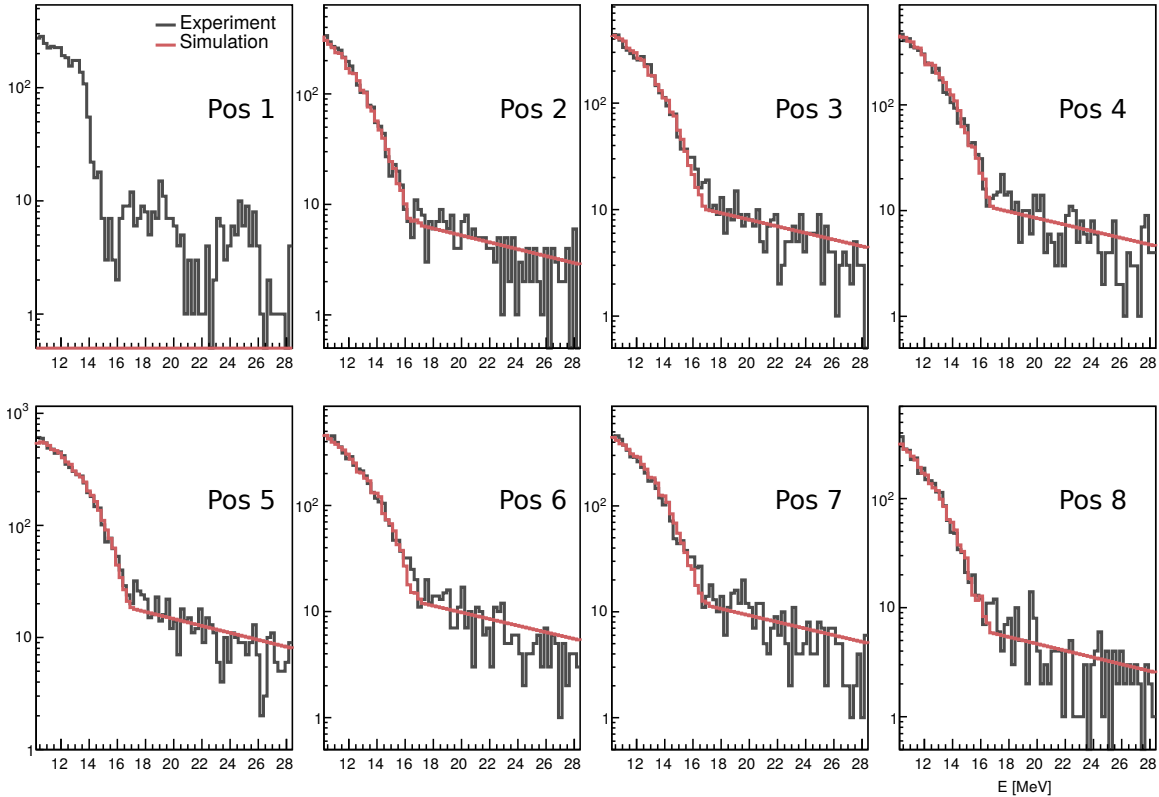
Figure 4.9: The calibrated energy spectra of the inner most ring of the PIN Array (black) and the simulated energy spectra (red) from Rutherford scattering. The PIN diode at position 1 was excluded from the fit and the rest of the analysis due to its unreliable energy response. See text below and Figure 4.10 for more detail.

The PIN diode at position 1 was excluded from the rest of the analysis because of its unreliable energy response. An example of the waveform output from this PIN diode is shown in Figure 4.10. For comparison, Figure 4.11 shows waveforms from the PIN diode at position 2 which had proper response.
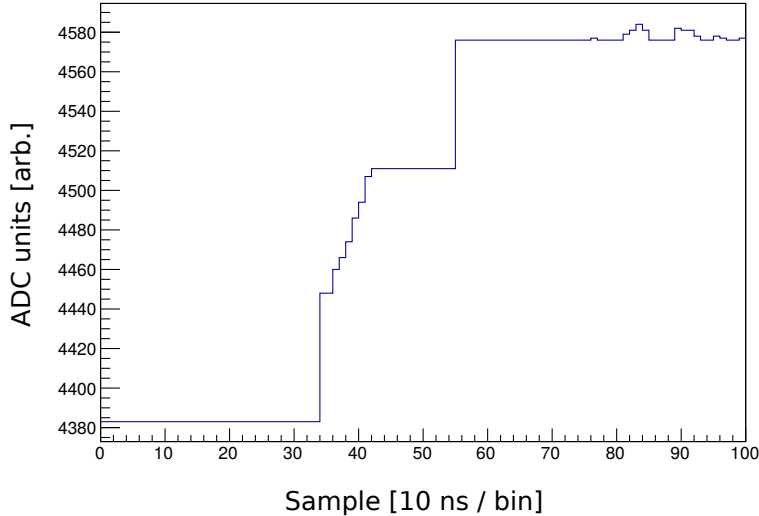
Figure 4.10: Example waveform from the position 1 PIN diode showing bad detector response. The normal response from another PIN diode is shown in Figure 4.11.

4.3 Particle Identification

The PIN Array was also capable of particle identification through analysis of the PIN diodes' waveforms. The type of radiation that was interacting with the PIN diode could be determined from the electronic response of the PIN diode. The signal waveform, $F(t)$, was fitted with functions described in Ref. [30],

$$
F(t) = C, \text{ for } t \leq t_0 ,
$$
$$
F(t) = C + A \left(1 - e^{-\frac{t-t_0}{\tau_{RT}}} \right) e^{-\frac{t-t_0}{\tau_{RC}}}, \text{ for } t > t_0 ,
$$

(4.9)

where t_0 is the start of the signal, C is the constant for the baseline, A is the amplitude of the waveform, τ_{RT} is the rise time of the signal, and τ_{RC} is the 50 μs decay time of the pre-amplifier. Figure 4.11 shows a comparison between the fits of the waveforms which resulted from a carbon-like particle hit versus an alpha-like hit. An elaborate description of the verification of this rise-time discrimination method can be found in Ref [30].

The rise time, τ_{RT} was fitted on an event-by-event basis for all the TIGRESS-PIN time-coincident data, which was then plotted with the calibrated incident particle energy into a 2-D histogram, shown in Figure 4.12. The correlation between incident energy and the rise time could be used as one of the ways to identify the type of the incident particle. This correlation is referred to as the particle ID (PID) in the rest of this thesis.

The intense regions of the PID plots in Figure 4.12 naturally separate into 3 clusters. The sharp, tall, and narrow cluster with rise time centred at 100 ns corresponds to hits from carbon-like particles. The cluster centred around (225 ns, 10000 keV) corresponds to hits
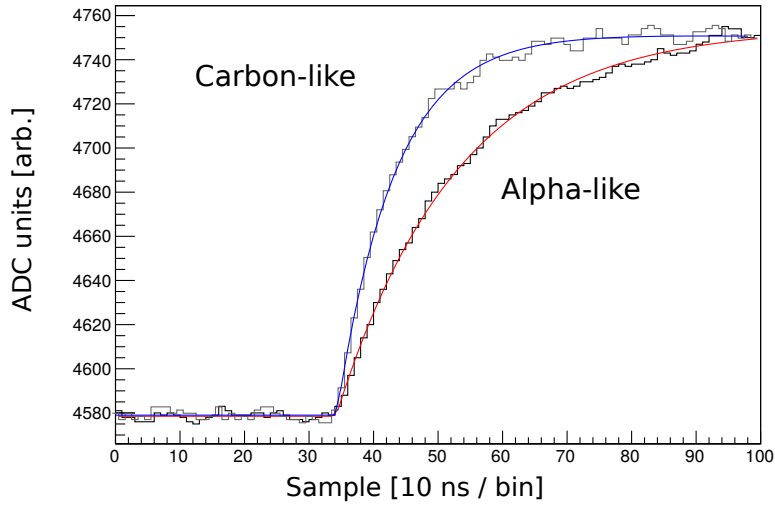
Figure 4.11: The waveforms fitted with Eq. 4.9 for a carbon-like particle (grey line with blue fit) and an alpha-like particle (black line with red fit).
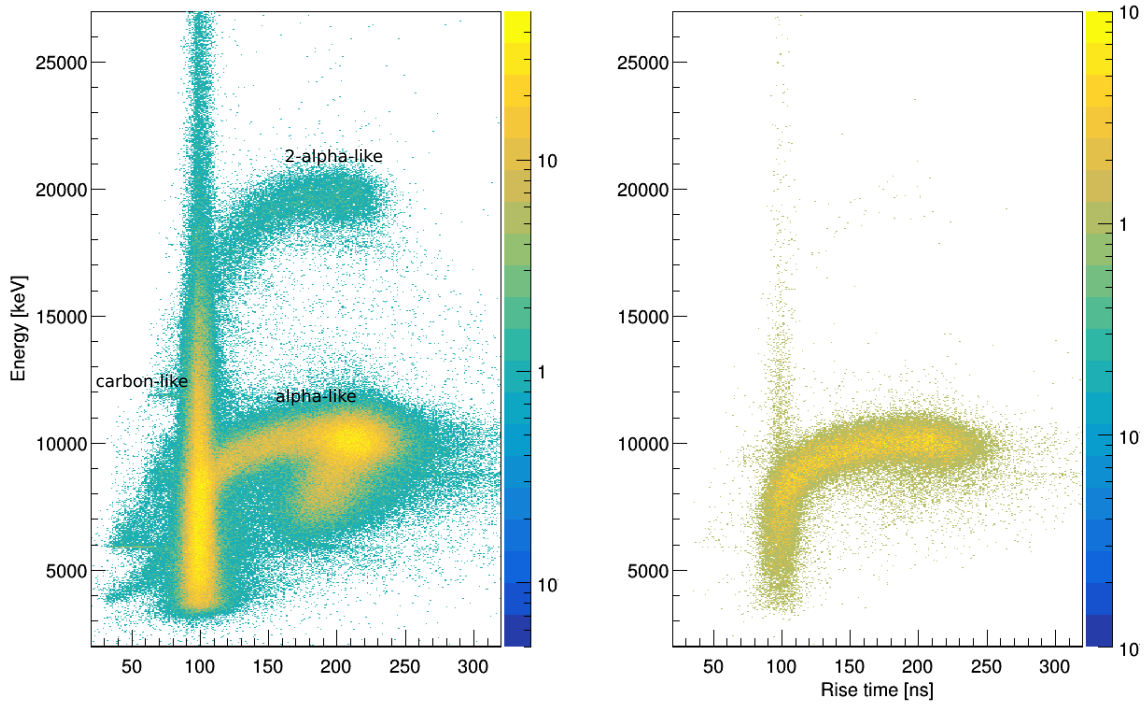
Figure 4.12: The energy-rise-time correlation (PID) histograms for the TIGRESS-PIN time-coincident data (left) and the time-coincident data selected for 2 hits in separate PIN diodes (right).

from alpha particles. Finally, the cluster centred around (225 ns, 20000 keV) corresponds to 2 alpha particles hitting a single PIN diode.

As a consequence of the time-coincidence method which is discussed in Section 2.6, falsely coincident events where charged particles from different processes were detected by separate PIN diodes in the same time window were rare. This meant that by imposing the PIN Array fold 2 gate, as described in Section 4.1.4, most events that passed the gate should be from the $(^{36}\text{Ar},2\alpha)$ reaction channel. This was verified with the PID plot sorted from the PIN Array fold 2 SFU files, shown in the right panel in Figure 4.12, where the majority of the events fell into the alpha-like region.

4.4   Analysis of Gamma-ray Spectra

This Section shows the progression of the gamma-ray spectra sorted using the various techniques that were discussed in the first half of this chapter. All of the gamma-ray spectra shown in this Section are sorted with Compton suppression and energy add-back, which were discussed in Sections 3.2.2 and 3.2.3, respectively. The top panel of Figure 4.13 shows the energy-calibrated gamma-ray spectrum summed over all TIGRESS detectors before enforcing time-coincidence. Each sub-section will show additional removal of unwanted events from the previous section.

4.4.1   TIGRESS-PIN Time Coincidence

The result of time coincidence, as described in Section 4.1.3, was the removal of the gamma ray peaks from Coulomb excitation of the gold backing which satisfied the DAQ's trigger condition through random coincidence. The middle panel of Figure 4.13 shows the TIGRESS-PIN time-coincident gamma-ray spectrum. The remaining peaks were all identified to be from gamma rays from the ^{36}Ar on $^{\text{nat.}}\text{C}$ reactions.

4.4.2   PIN Array Fold and PIN-PIN Time Coincidence

Reaction channel selection for ^{40}Ca was achieved by selecting for events with PIN Array fold 2, as described in Section 4.1.4. Additionally, false coincidence in the PIN singles were reduced as described in Section 4.1.5. The bottom panel in Figure 4.13 shows the gamma-ray spectrum that is time-coincident and has 2 separate PIN signals within 40 ns. All visible peaks here came from transitions in ^{40}Ca. Gamma-ray spectra sorted from these events will be the basis for the rest of this Chapter.

4.4.3   Doppler Correction

The short lifetimes of the 4_1^+ and 2_1^+ states in ^{40}Ca relative to its stopping time in the gold backing meant that gamma rays that were emitted from the decay of these states experienced significant Doppler shifts as described in Section 4.1.6. The effect of Doppler shift can be seen in the bottom panel of Figure 4.13, where the 4^+ (to 2^+) peak was broadened and the 2^+ (to 0^+) transition was split into 3 peaks.

Figure 4.13: The energy-calibrated gamma-ray spectrum, with Compton suppression and energy add-back, sorted from the full data before enforcing time-coincidence (top), after TIGRESS-PIN time-coincidence (mid), and the time-coincidence data further selected for PIN Array fold 2 with PIN-PIN time-coincidence (bottom). Each bin in each histogram is 4 keV wide.

The Doppler-shifted energies of the 2^+ and 4^+ peaks can be corrected into the gamma-ray energy in the frame of the ^{40}Ca by rearranging Equation 4.4,

$$E_0 = E_\gamma / D \ . \tag{4.10}$$

Correcting for Doppler shift this way made it possible to show the sum intensities of the Doppler-shifted peaks within a single spectrum. The drawback was that the fully stopped

peaks from longer-lived states were washed out. Figure 4.14 shows the Doppler-shift corrected gamma-ray spectrum sorted from the events described in Section 4.4.2. The signifi-

Figure 4.14: The energy-calibrated, Doppler-shift corrected gamma-ray spectrum sorted from the PIN Array fold 2, PIN-PIN time-correlated SFU file as described in Section 4.4.2. Each bin in the histogram is 4 keV wide.

cant narrowing of the 2^+ and 4^+ peaks compared to Figure 4.13 also serves as verification for the calculated Doppler-shift factors, described in Section 4.1.6.

The Doppler-corrected 2^+ peak has 2360 ± 70 counts and the 4^+ peak 340 ± 30 counts. Before correcting for the difference in TIGRESS efficiencies at different energies, the 2^+ peak is 6.9 ± 0.7 times more intense than the 4^+ peak. After correcting for the energy-dependent detector efficiency, which was described in Section 4.2.2, using the most-conservative lower bound of the efficiency ratio of $3:1$, the ratio of $2^+:4^+$ becomes $21(\pm2):1$. This means that for every 21 events in the 2^+ peak, only 1 came from the feeding through 4^+ while the other 20 were from the direct population of 2^+. On the other extreme, the ratio of $2^+:4^+$ becomes $35(\pm4):1$ if the $5:1$ upper bound of the efficiency ratio was used.

4.4.4   PIN Array Energy Correlation

The energy correlation of the two alpha particles, shown in Figure 4.15, was a result of the reaction mechanism which produced the excited ^{40}Ca. It can be used to further enhance the ratio of direct population of the 2^+_1 state. Selecting events that fell into each depicted gate enhanced the relative intensity of the respective gamma-ray transition.

The gamma-ray spectrum sorted from the events in the 2^+ gate is shown in the top panel and the 4^+ in the bottom panel of Figure 4.16. With the 2^+ gate the efficiency-corrected ratio of $2^+:4^+$ is $35(\pm7):1$ (or $60(\pm10):1$ using the upper-bound of the efficiency factor). With the 4^+ gate the ratio is $16(\pm3):1$. To minimize the effect of feeding, extraction of the 2^+ lifetime will be based on the 2^+ gated events. Because the reaction was sub-barrier,
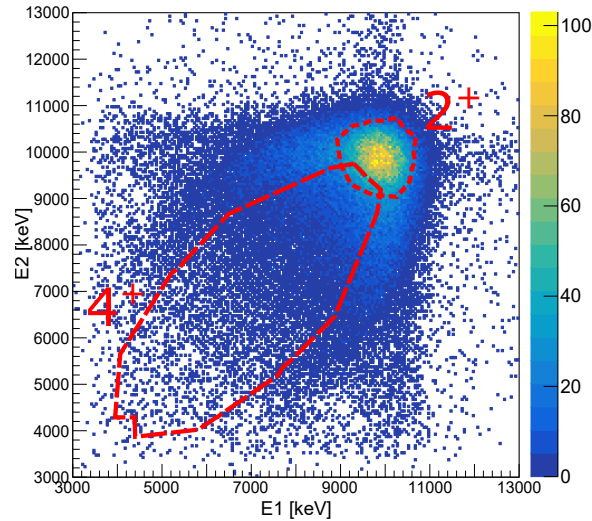
Figure 4.15: The symmetrized energy correlation of the two PIN Array signals in an SFU event. The dotted lines represent gates on the energy correlation that would enhance the relative gamma ray intensity from the states that are labeled.

as described in Section 2.1, and no gamma-ray peaks were observed to transition into 4^+, there is little concern for feeding into the 4^+ state. In addition, the Compton background from the 2^+ peak was not intense as shown in Figure 4.14. Therefore all the events that satisfied the conditions in Section 4.4.2 will be used for the lifetime extraction of the 4^+ state.

4.4.5 Doppler-Shift Measurements of the 4^+ and 2^+ Transitions in ^{40}Ca

The lifetime of an excited state can be extracted using DSAM from the amount of Doppler shift, as described in Section 2.5. In addition to the broadening of the 2^+ and 4^+ peaks in Figure 4.13, the Doppler shift of these peaks can be quantified by sorting the data into Doppler-shift groups that are shown in Figure 4.6 and defined in Section 4.1.6. The gamma-ray spectra sorted by Doppler-shift groups are shown in the vertical panels of Figure 4.17. The events in the left panels of Figure 4.17 were sorted from all events that satisfied the conditions in Section 4.4.2, while the right panels had the additional 2^+ gate which was described in Section 4.4.4. Gamma-ray peaks corresponding to the shorter-lived 4^+ and 2^+ states in Figure 4.17 are misaligned across the vertical panels as a result of Doppler shift, while the longer-lived 0^+ and 3^- peaks have constant energies that align across Doppler-shift groups.

The un-gated spectra in the left panel of Figure 4.17 are used for the lifetime extraction of the 4^+ state in ^{40}Ca, and the 2^+ gated spectra in the right panel are used for extraction of its 2^+ lifetime. Method and analysis of the lifetime extraction will be discussed in Chapter 5.
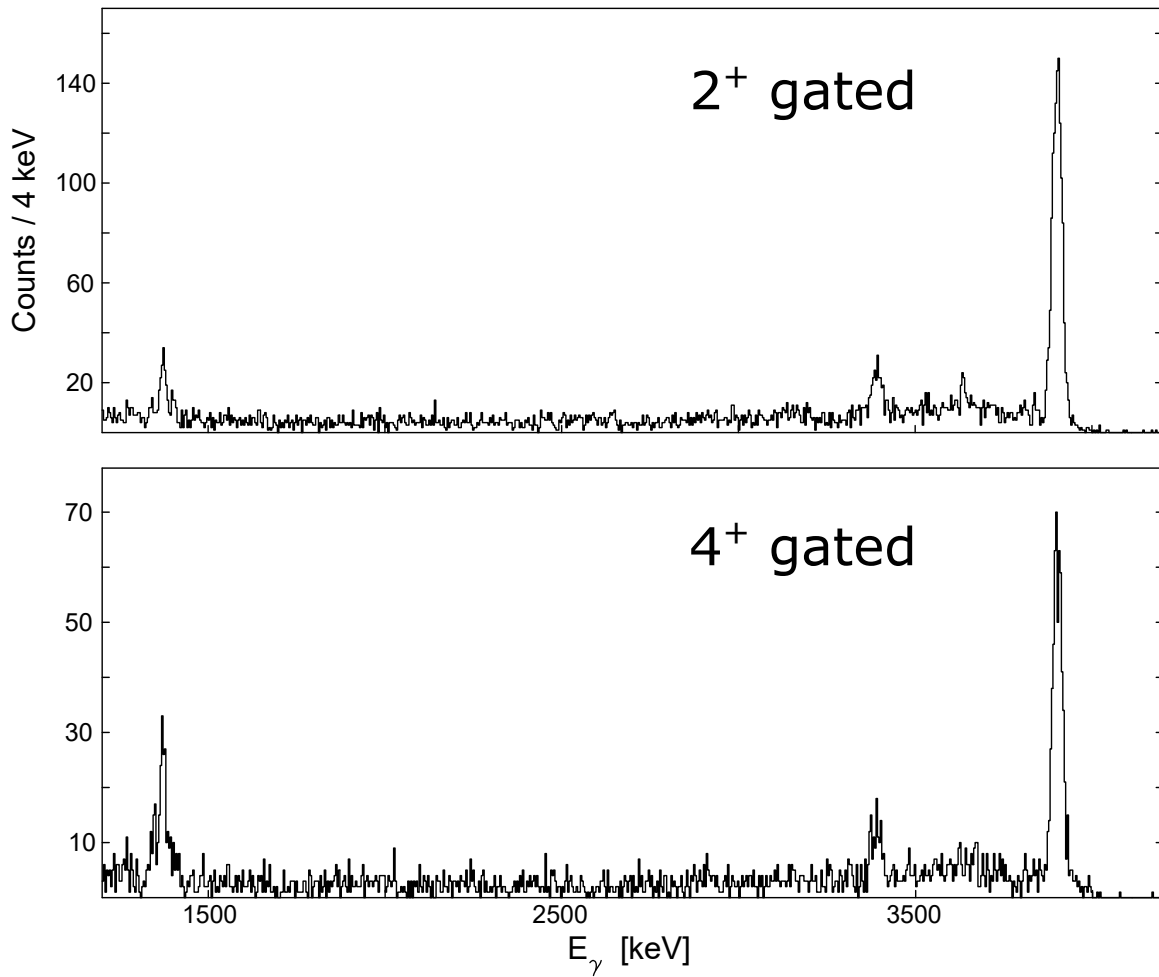
Figure 4.16: The energy-calibrated, Doppler-shift corrected gamma-ray spectra sorted from the PIN Array fold 2, PIN-PIN time-correlated SFU file, with additional 2^+ (top) and 4^+ (bottom) gates on alpha-alpha energy correlation as shown in Figure 4.15. Each bin in each histogram is 4 keV wide.
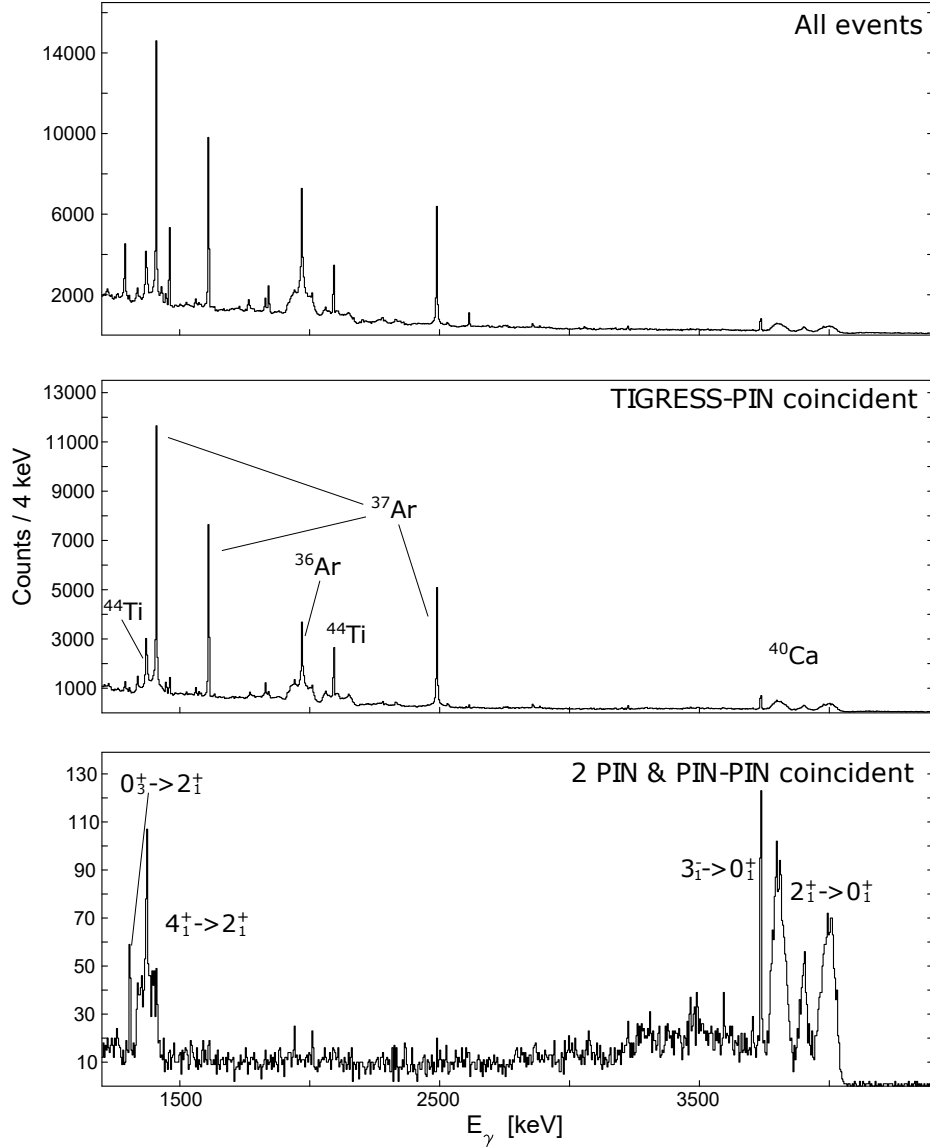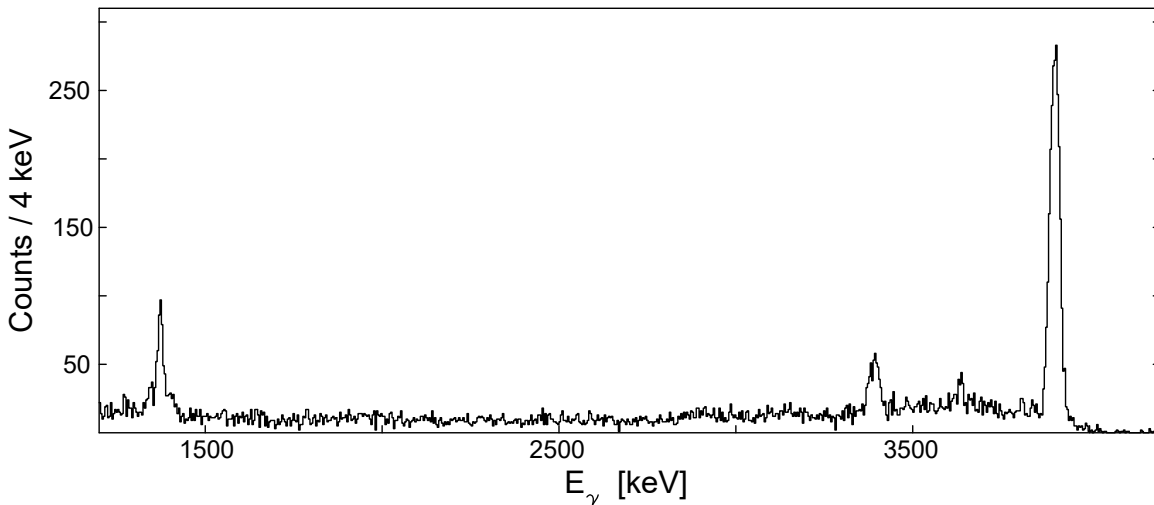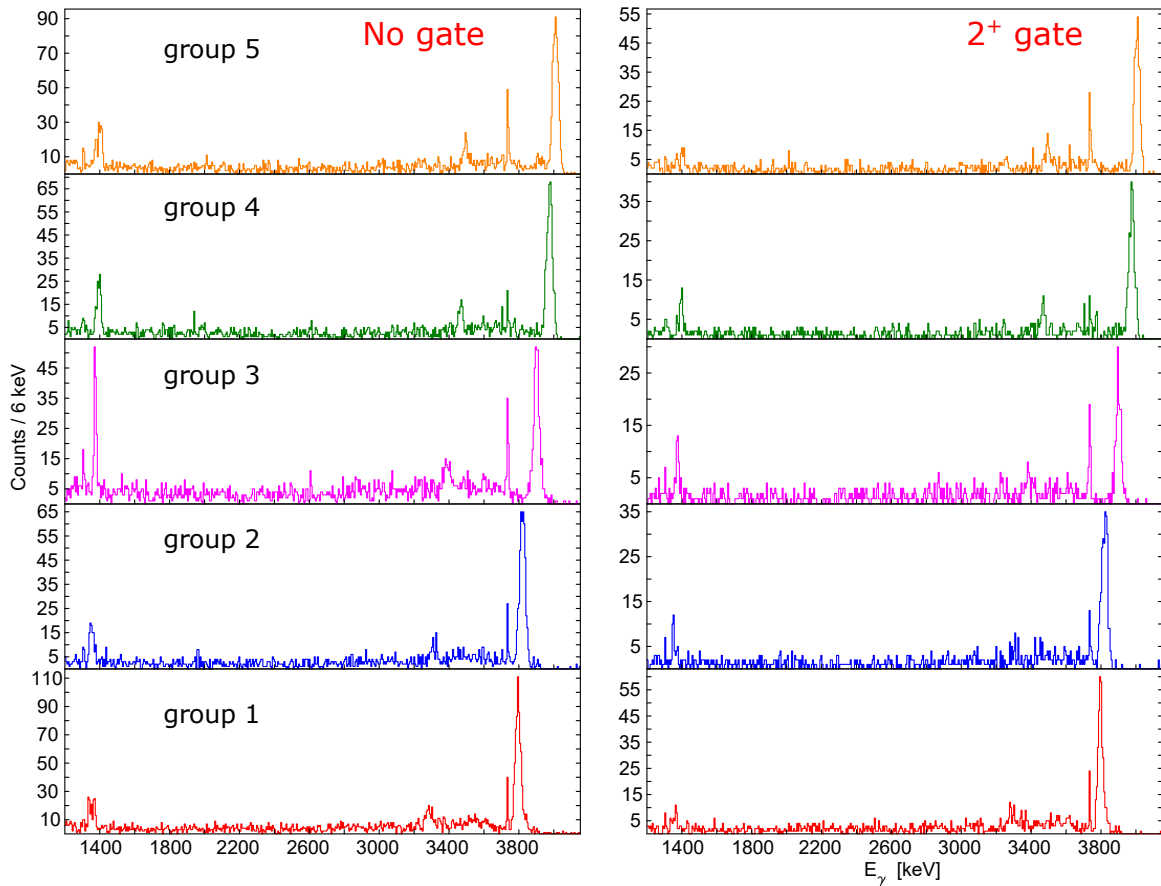
Figure 4.17: The energy-calibrated gamma-ray spectrum, with Compton suppression and energy add-back, sorted for events with PIN Array fold 2 and PIN-PIN time coincidence without (left) and with (right) the alpha-alpha energy correlation gate for 2^+, as shown in Figure 4.15. The vertical panels represent different Doppler-shift groups, as defined in Section 4.1.6. Each bin in each histogram is 4 keV wide.

Chapter 5

GEANT4 Simulations

The lifetimes of the 4_1^+ and 2_1^+ states in ^{40}Ca are on the order of tens of fs to ps, which are orders of magnitude shorter than the response time of the detectors or the DAQ's 100 MHz clock. This means that theses lifetimes cannot be measured directly from the decrease of activity over time. Instead, they were measured indirectly with respect to the stopping of ^{40}Ca and the Doppler shift of gamma rays using DSAM, as described in Section 2.5. The lifetimes of theses excited states were encoded in the line shapes of the gamma-ray spectra, which were also impacted by other factors such as the reaction mechanism, the stopping process of the ^{40}Ca and the geometry of the experimental setup. To account for these factors in a consistent and reproducible way, a software for Monte-Carlo simulation was developed within the GEANT4 [38] framework. The software allowed the user to input parameters for physical processes, such as the lifetimes of the excited states and the reaction mechanism, and simulated these processes, while obeying momentum and energy conservations from the generation of the beam particles to the interaction of the reaction products with the detector systems. Information about the energy deposition into the detector systems were recorded in a ROOT [39] file, which would be later converted into spectra analogous to the ones that were described in Chapter 4.

To determine the best-fit value for each parameter, a series of simulations were completed with a range of different possible parameter values. The simulated results for each parameter were then fitted to their experimental counterparts using the maximum likelihood method, as described in Ref [40], and the calculated χ^2 goodness of fit value was plotted as a function of the parameter values. The χ^2 vs. parameter value plot was then fitted using a polynomial function to determine the value which gave the minimum χ^2. The fitted value with minimum χ^2 was defined to be the best-fit value of the parameter. The 1σ uncertainty of the parameter was determined to be the x-values bound by the polynomial fit at $\chi^2_{\min} + 1$ [41]. If the model that was input to the simulations describes the process perfectly, it is expected that $\chi^2_{\min} \sim \nu$, where ν is the number of degrees of freedom. If $\chi^2_{\min} > \nu$, the 1σ uncertainty was inflated by a factor $\sqrt{\chi^2_{\min}/\nu}$, as recommended by the Particle Data Group [42], to account for the deficiencies in the model.

5.1 Rutherford Scattering

Rutherford scattering is the elastic scattering of two nuclei, which is well-understood. It was also the process that has the greatest cross section among the ones that are discussed in this thesis. In the centre of mass, for a given pair of beam and target nuclei, the scattering cross section depends on the velocity of the beam, v, and the scattering angle, θ [43],

$$\frac{d\sigma}{d\Omega} = \left(\frac{kZ_BZ_Te^2}{2\mu v^2}\right)^2 \frac{1}{\sin^4(\theta/2)} , \tag{5.1}$$

where k is the electromagnetic coupling constant, e is the elementary charge, μ is the reduced mass, and Z_B and Z_T are respectively the atomic numbers of the beam and target nuclei.

The Rutherford scattering between the beam and target nuclei was implemented in GEANT4 as following:

1. The beam nucleus is generated by the GEANT4 particle gun at a user-specified energy 50 mm upstream the target face.

2. The beam nucleus experiences straggling and energy loss once it enters the target, until it reaches a randomized depth. This becomes the position of the Rutherford interaction.

3. The beam nucleus is assigned a direction isotropically in the centre of mass and assigned a weight that corresponds to the reaction cross section, as described in Equation 5.1. Simulated spectra constructed for analysis are incremented by the weight to account for the dependence of the scattering cross section on the scattering angle and the incident energy.

4. The target nucleus is assigned momentum following conservation laws.

5. Both the beam and target nuclei are handed back to GEANT4 as secondaries at the point of interaction, inheriting the weight calculated in step 3.

Simulations of Rutherford Scattering were used to verify the thickness of the gold backing and the energy calibration of the PIN Array. The simulated PIN Array energy spectrum with the correct backing thickness is expected to match the experimental PIN Array energy spectrum with the correct energy calibration.

Rutherford scattering with a range of thicknesses of the gold backing was simulated, and the resulted spectra for each PIN diode in Ring 1 (except position 1) was fitted to the experimental data with the constraint that all the 7 spectra share the same scaling factor. The χ^2 plotted as a function of the backing thickness is shown in Figure 5.1. The best-fit backing thickness was 11.799 μm, with the $\chi^2_{\min}/\nu = 1.6$. The 1σ bound extracted from $\chi^2_{\min} + 1$ was ± 0.011 μm. This was then scaled by $\sqrt{\chi^2_{\min}/\nu} = 1.27$ to ± 0.014 μm. The final

reported thickness was 11.8 ± 0.01 μm. The comparison between the simulation at 11.8 μm and the experimental spectra is shown in Figure 4.9.
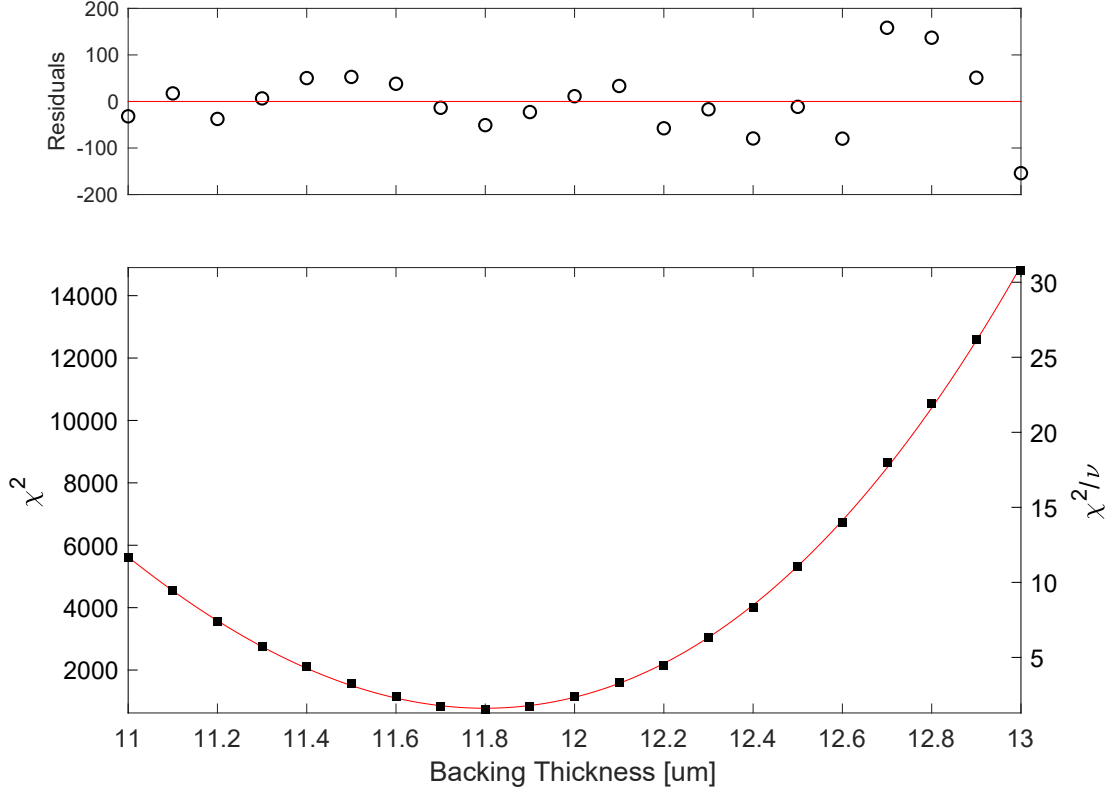
Figure 5.1: The χ^2 calculated from the simulated and experimental PIN spectra in Ring 1 for Rutherford scattering, plotted against the backing thickness that was used in the simulation. The red line is a cubic fit with the minimum at 11.8 ± 0.1 μm and $\chi^2_{\min}/\nu = 1.6$.

5.2 The Alpha-Transfer Reaction Mechanism

The reaction mechanism that populated the excited states in ^{40}Ca can also be inferred by comparing the PIN Array hit information simulated from a proposed reaction mechanism to the experimental data. Simulation with the correct reaction mechanism is expected to reproduce the angular and energy distributions that were seen in the experiment. The reaction model forms ^{40}Ca by transferring one of the three alpha particles from the ^{12}C core to the ^{36}Ar. To maximize its flexibility, the reaction mechanism is illustrated in Figure 5.2 and implemented as the following:

1. The ^{40}Ca was created in an excited state with user-defined excitation energy and lifetime.

2. In the centre of mass, ^{40}Ca and the 2-alpha cluster were formed with scattering angle θ and take equal and opposite momenta of $\pm\vec{p}$, respectively. The magnitude of the momenta was determined by energy conservation, as described in Equation 2.10. The scattering angle was initially generated isotropically and recorded for each event, which can be used to bias the events after the simulation.

3. The alpha particles in the cluster each take momenta such that their sum momentum is equal to $\vec{p}$. It was parameterized that the momentum of each alpha particle was the sum of $\vec{p}/2$, plus/minus a perpendicular component, $\vec{p}_{\text{short}}$. The ratio of $\vec{p}_{\text{short}} : \vec{p}/2$ was called x, which was a free parameter that was input by the user. The magnitude of $\vec{p}$ was then determined from the conservation of energy and momenta.

4. The products were created as secondary particles in GEANT4, boosted back to the LAB frame, and added to the track.

In the centre of mass:
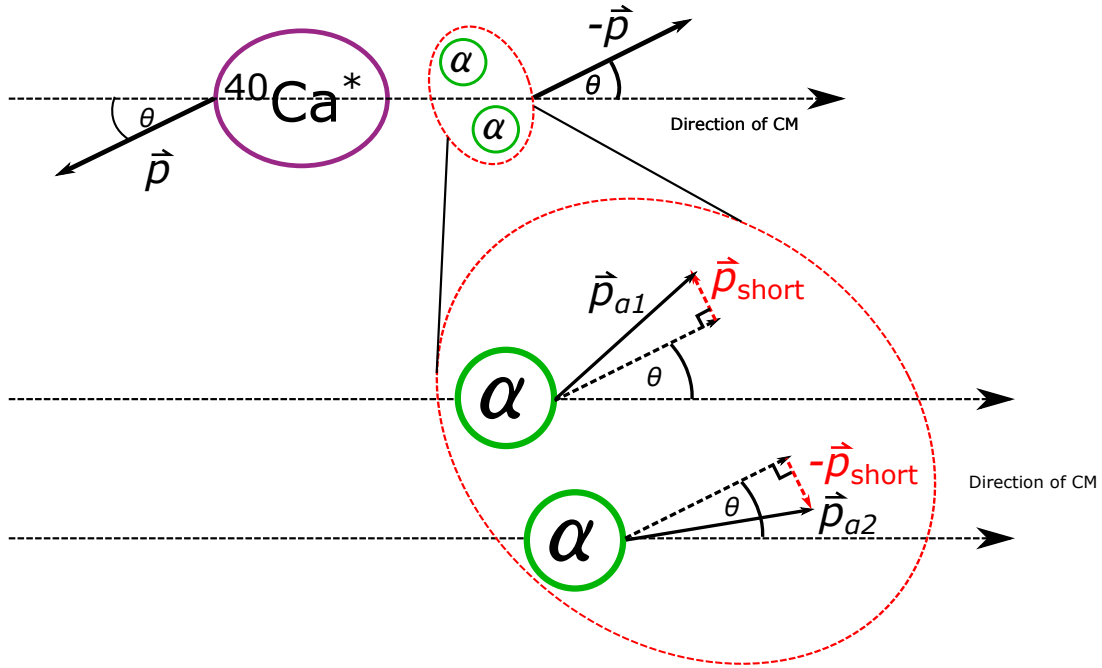
Figure 5.2: The alpha-transfer reaction mechanism. In the centre of mass, the excited ^{40}Ca and the 2-alpha cluster scatter at angle θ with opposite momenta of the same magnitude, p. The 2 alpha particles each have half of p, which was then added by a perpendicular component, $\pm\vec{p}_{\text{short}}$ to account for the internal excitation of the cluster.

Because the reaction mechanism determines the initial velocity distribution of the ^{40}Ca, having the reaction parameters that are consistent with the experimental data is critical for DSAM lifetime measurements.

5.2.1 Reaction Parameters

In general, θ controls the intensity of the oval "tails" into the low energy in the PIN Array energy correlation plot, and x controls the amount of anti-diagonal opening of the two tails. Values for these parameters were chosen to qualitatively best resemble the charged particle data to establish the initial momentum distribution of the excited ^{40}Ca. Example plots of PIN Array energy correlations resulted from different parameter combinations are shown in Figure 5.3. No combination of these parameters were found that would properly reproduce the energy correlation in Figure 4.15. In particular, the simulation always had too much energy in the alpha particles. Discussion on this disagreement can be found in Chapter 6.
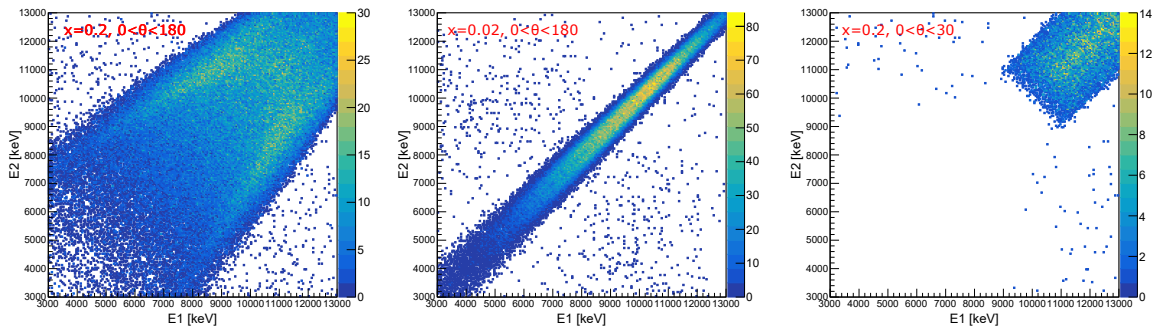
Figure 5.3: Example PIN Array energy correlations as a result of reaction parameter choices. Definition of these parameter can be found in the text. In general increasing x opens the oval "tails", and constraining to low θ eliminates the low-energy tails.

5.3 The Determination of Lifetimes

Because no combination of the reaction parameters were found to fully reproduce the experimental PIN Array energy correlations, $x = 0.01$ and θ from 0 to 180 degrees were chosen for the analysis in this section as a placeholder. After the excited ^{40}Ca was produced by the reaction mechanism that was described in Section 5.2, it continued to be tracked in GEANT4 until it decayed via the emission of gamma ray following a user specified lifetime. TIGRESS gamma-ray spectra were simulated this way with a range of lifetimes, and the result for each lifetime was fitted to the experimental spectra sorted by the Doppler shift factors, as described in Section 4.1.6. The lifetime that was inputted to simulate the spectra which provided the lowest χ^2 when fitted to the experimental data was determined to be the best-fit lifetime. The lifetimes that are reported in this Section are limited by the incomplete reaction mechanism. The reaction mechanism affected DSAM lifetimes because it determined the initial velocity distribution of the ^{40}Ca. Determination of the complete reaction mechanism is beyond the scope of this thesis, and will likely require further experiments. These limitations are discussed further in Chapter 6.

5.3.1 Lifetime of the 4_1^+ State

Gamma-ray spectra were simulated in GEANT4 with a range of lifetimes of the 4_1^+ state in ^{40}Ca. The simulated gamma-ray line shapes with each lifetime were scaled and fitted to the experimental line shapes in each Doppler-shift group with a linear background. The χ^2 was summed from all five Doppler-shift groups, and plotted against the input lifetime in Figure 5.4. The best-fit lifetime was determined to be 273 fs with $\chi^2_{\min}/\nu = 1.36$ by fitting a cubic polynomial. The 1σ bound extracted from $\chi^2_{\min} + 1$ was $^{+11}_{-12}$ fs. This was scaled by $\sqrt{\chi^2_{\min}/\nu} = 1.17$ to $^{+13}_{-14}$ fs to account for the fit's $\chi^2_{\min}/\nu > 1$. The final reported lifetime from this measurement was 270 ± 10 fs after rounding for significant figures. The best-fit
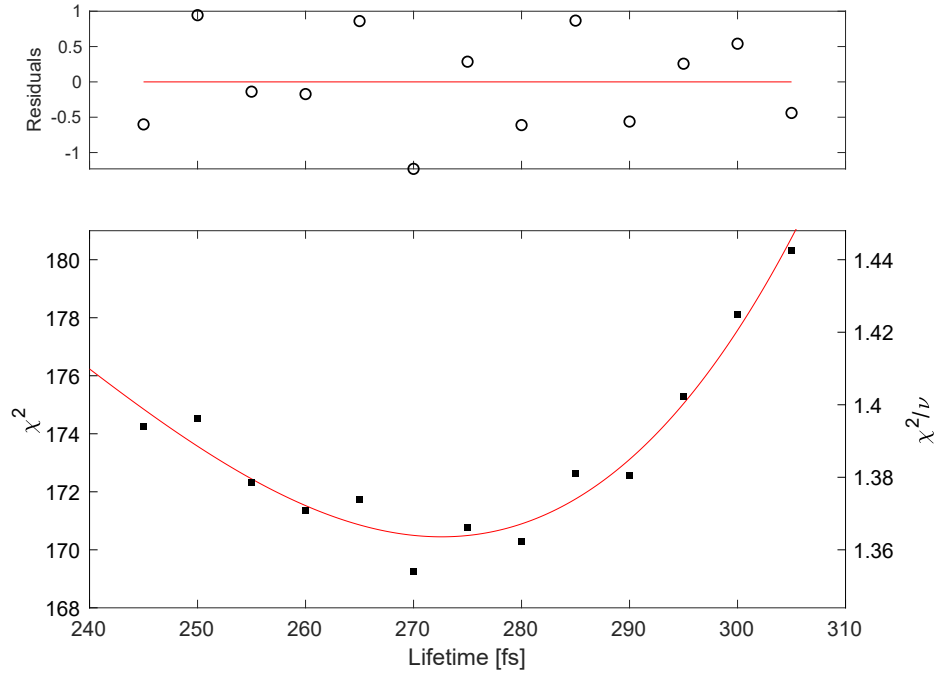
Figure 5.4: The χ^2 from fitting the simulated to the experimental gamma-ray line shape, summed over all Doppler shift groups and plotted against the lifetime of the 4_1^+ state in ^{40}Ca that was used in each simulation. The red line is a cubic polynomial fit with the minimum at 270(10) fs and $\chi^2_{\min}/\nu = 1.36$.

gamma-ray line shape with comparison to experimental data is shown in Figure 5.5.

5.3.2 Lifetime of the 2_1^+ State

Following the identical procedure as in Section 5.3.1, the χ^2 summed for all Doppler-shift groups is plotted as a function of the 2_1^+ lifetime in Figure 5.6. The best-fit lifetime was determined to be 42.5 fs with $\chi^2_{\min}/\nu = 2.1$ by fitting a cubic polynomial. The 1σ bound extracted from $\chi^2_{\min} + 1$ was $^{+3.5}_{-3.4}$ fs. This was scaled by $\sqrt{\chi^2_{\min}/\nu} = 1.45$ to $^{+5.1}_{-4.9}$ fs to account for the fit's $\chi^2_{\min}/\nu > 1$. The final reported lifetime from this measurement was 42 ± 5 fs after rounding for significant figures. The best-fit gamma-ray line shape with comparison to
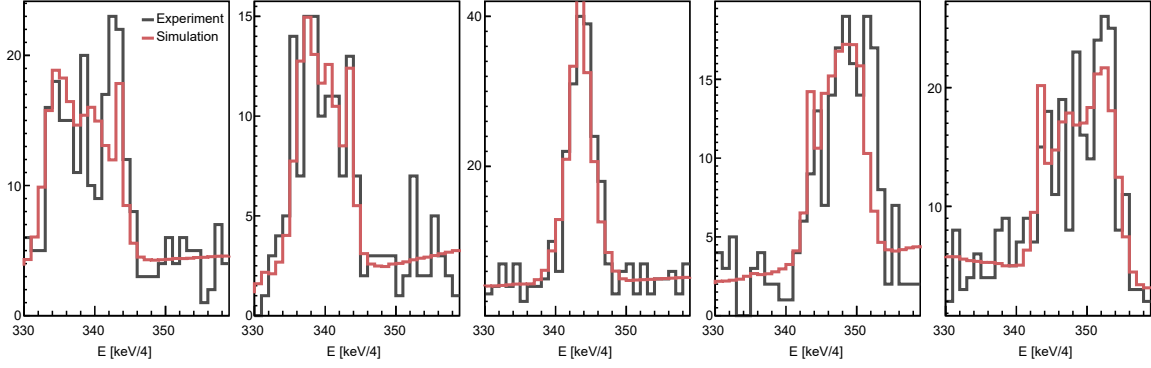
Figure 5.5: The best-fit simulated (red) line shapes scaled to fit on the experimental ones, for the $4_1^+ \rightarrow 2_1^+$ transition in ^{40}Ca. The 4_1^+ lifetime used to generate the simulated line shapes was 270 fs. The panels from left to right are Doppler-shift groups 1 to 5.
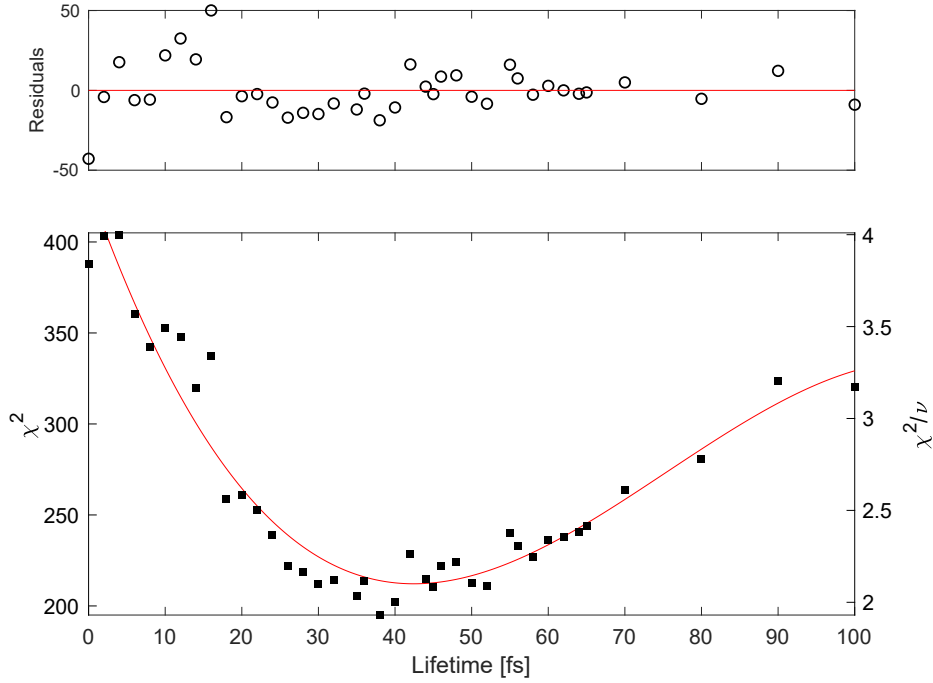
Figure 5.6: The χ^2 from fitting the simulated to the experimental gamma-ray line shape, summed over all Doppler shift groups and plotted against the lifetime of the 2_1^+ state in ^{40}Ca that was used in each simulation. The red line is a cubic polynomial fit with the minimum at 42(5) fs and $\chi^2_{\mathrm{min}}/\nu = 2.1$.

experimental data is shown in Figure 5.7. In the middle panel of this figure, the simulated line shape is significantly wider than the experimental one for $D \sim 1$. This is likely a result of the incomplete reaction mechanism and will be discussed further in Chapter 6.
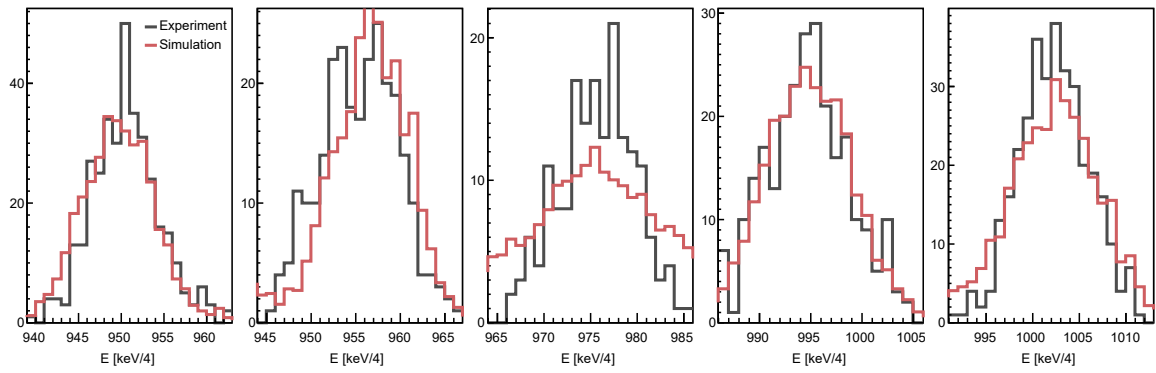
Figure 5.7: The best-fit simulated (red) line shapes scaled to fit on the experimental ones, for the $2_1^+ \rightarrow 0_1^+$ transition in ^{40}Ca. The 2_1^+ lifetime used to generate the simulated line shapes was 42 fs. The panels from left to right are Doppler-shift groups 1 to 5.

Chapter 6

Discussion and Future Work

6.1 Discussion

Direct population of the 2_1^+ state was achieved with a direct-population-to-feeding ratio of $21(\pm2) : 1$. This ratio increases to $35(\pm7) : 1$ after gating in the charged-particle energy correlation. The 2_1^+ lifetime that was measured in this experiment was 42 ± 5 fs, and the 4_1^+ lifetime was 270 ± 10 fs. Both uncertainties quoted here are statistical only. Figure 6.1 shows these results in comparison to literature values.
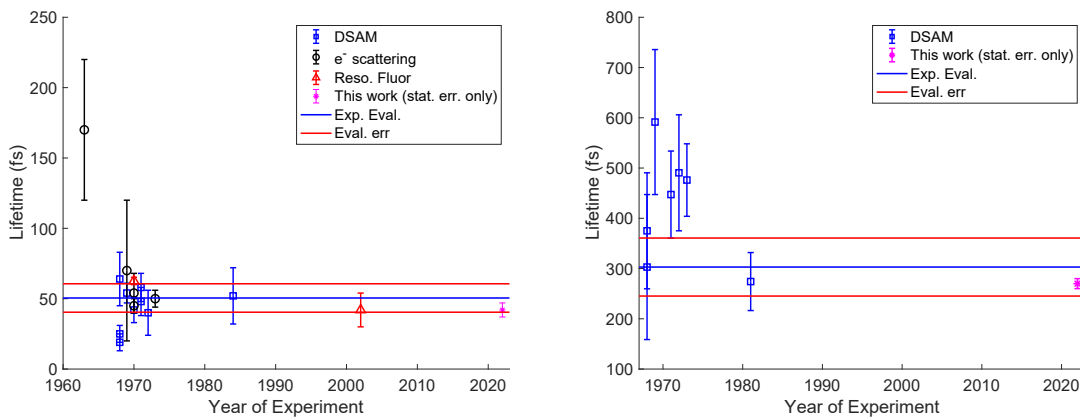
Figure 6.1: Lifetimes of the 2_1^+ (left) and 4_1^+ (right) states in ^{40}Ca. This is a reprint of Figures 1.2 and 1.3 with results of this work added as magenta stars. Note: the error bars for this work contain statistical uncertainties only.

The question that is left unanswered is: what was the underlying reaction mechanism that populated the 2_1^+ and 4_1^+ states in ^{40}Ca? Although the reaction mechanism that was proposed in Section 5.2 qualitatively reproduced some features in the PIN Array energy correlation, the sum energy of the alpha particles was still too high regardless of the reaction parameter choices. Constrained by the conservation of energy, the excess energy in the alpha particles must go into something else.

Because the energy available in the centre of mass (after accounting for the Q-value) was 15.51 MeV, exciting ^{40}Ca to a higher-energy state may seem to be a good placement of this energy. However, transitions from those higher-lying states to the 4_1^+ or 2_1^+ were not observed in the gamma-ray spectra with sufficient intensities.

Since the target was composed of $^{nat.}$C, the ^{36}Ar might have reacted on ^{13}C instead of ^{12}C. If this were true, the excess energy could have been carried away by the additional neutron. But why would the reaction favour the 1.1% abundant ^{13}C over the 98.9% abundant ^{12}C?

Finally, this could all be an artifact of a miss-calibrated PIN Array. After all, the ^{40}Ca reaction channel was not the intended reaction of study when this experiment was performed. As a result, the PIN array was never calibrated with high-energy alpha particles. As described in Section 4.2.3, the PIN Array was calibrated with the triple-alpha source and then verified with Rutherford scattering of ^{12}C. However, this calibration is not bullet-proof. The maximum energy of the triple-alpha source is 5.8 MeV, which is only $\sim 50\%$ of the alpha energy from the transfer reaction. Because the DSAM target had a gold backing, and the thickness of the backing was also fitted as a parameter using the Rutherford scattering of ^{12}C, the agreement in the Rutherford scattering spectra could just be a coincidence, where the miss-calibration was masked by the free-floating backing thickness. In addition, the energy calibration may be different for alpha particles versus carbons due to the ion-specific detector responses.

Because of the limitations listed above and the lack of agreement between the simulated and experimental PIN Array energy correlation, the initial velocity distribution of the ^{40}Ca cannot be constrained. As a result, it is prohibitive to determining the systematic uncertainties for the DSAM lifetimes that are reported in Chapter 5.

6.2   Future Work

Despite limitations in constraining the reaction mechanism, examination of the experimental gamma-ray spectra showed clear evidence for the direct population of the 2_1^+ and 4_1^+ states in ^{40}Ca. This reaction mechanism is therefore worth studying further, not only for the proper extraction of the lifetimes, but also for a better understanding of the alpha-transfer reaction mechanism. To eliminate the ambiguities that are discussed in Section 6.1, the experiment should be repeated with isotopically pure carbon targets and proper charged-particle energy calibration using the Rutherford scattering of accelerated alpha particles.

6.3   Added After the Defence

Investigation of the reaction mechanism continued after the submission of this thesis to the examining committee. The experimental alpha-energy correlation was produced in the newly proposed reaction mechanism, as shown in Figure 6.2. In this new reaction mechanism, the
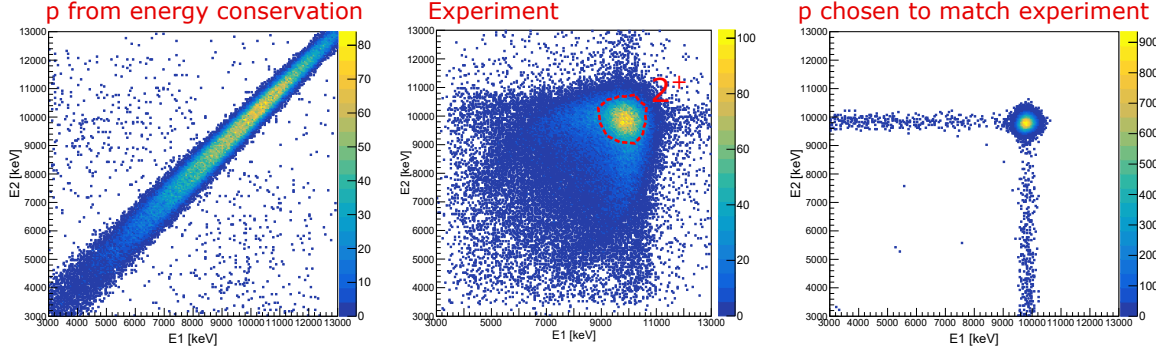
Figure 6.2: The symmetrized PIN Array energy correlations from the reaction mechanism described in Section 5.2 (left), the experiment (centre), and the newly proposed reaction mechanism (right).
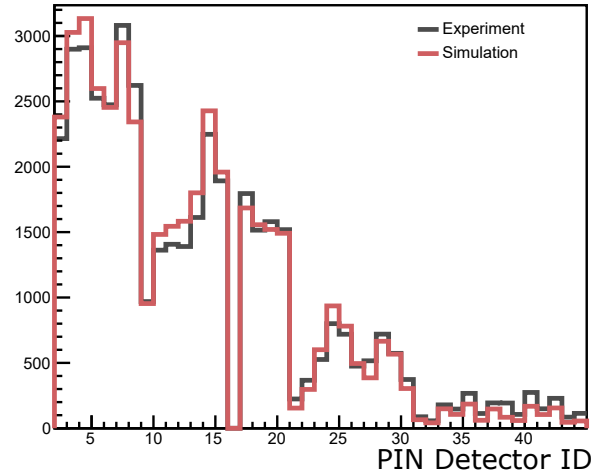
Figure 6.3: The fold-2 PIN Array hit pattern from the simulation (red) and the experiment (black). The scattering angle was biased in the simulation to reproduce the experimental distribution.

magnitude of the ^{40}Ca momentum is no-longer determined by energy conservation as in the original mechanism described in Section 5.2. In contrast, the magnitude of the momentum was chosen phenomenologically to match the experimental alpha-energy correlation. Instead of enforcing energy conservation among the alpha particles and the ^{40}Ca at discrete excited states, the new model accepts that the reaction process irradiated some energy that was not observed in the detector systems. That said, the new mechanism still enforces momentum conservation, which means that the initial momentum distribution of the ^{40}Ca is still constrained by the charged-particle hit information. In addition to reproducing the alpha energy correlation, this new mechanism can also reproduce the angular distribution of the alpha particles, verified by the PIN Array hit pattern shown in Figure 6.3.

It is expected that this new reaction mechanism will improve the constraint in the initial momentum distribution of the ^{40}Ca, which will consequently improve the agreement between the simulated and experimental gamma-ray spectra shown in Figure 5.7.

The reason for the non-observation of the energy difference is still being actively investigated at the time of this thesis' submission.

Bibliography

[1] C. J. Van Oss, M. K. Chaudhury, and R. J. Good, "Interfacial Lifshitz-van der Waals and polar interactions in macroscopic systems," *Chem. Rev.*, vol. 88, pp. 927–941, Sept. 1988.

[2] T. Otsuka, T. Suzuki, J. D. Holt, A. Schwenk, and Y. Akaishi, "Three-Body Forces and the Limit of Oxygen Isotopes," *Phys. Rev. Lett.*, vol. 105, p. 032501, July 2010.

[3] P. Navrátil, R. Roth, and S. Quaglioni, "Ab initio many-body calculations of nucleon scattering on ^{4}He, ^{7}Li, ^{7}Be, ^{12}C, and ^{16}O," *Phys. Rev. C*, vol. 82, p. 034609, Sept. 2010.

[4] G. Audi, "The History of Nuclidic Masses and of their Evaluation," *International Journal of Mass Spectrometry*, vol. 251, pp. 85–94, Apr. 2006. arXiv: physics/0602050.

[5] B. A. Brown, *Lecture Notes in Nuclear Structure Physics*. National Superconducting Cyclotron Laboratory and Department of Physics and Astronomy Michigan State University. `http://nuclear.fis.ucm.es/PDFN/documentos/BAB-lecture-notes-NUCLEAR-PHYSICS.pdf`, Accessed: 2022-07-13.

[6] K. L. G. Heyde, *The nuclear shell model / Kris L.G. Heyde.* Springer series in nuclear and particle physics, Berlin ; New York: Springer-Verlag, 1990.

[7] J. Chen, "Nuclear Data Sheets for A=40," *Nuclear Data Sheets*, vol. 140, pp. 1–376, Feb. 2017.

[8] M. G. Mayer, "On Closed Shells in Nuclei," *Phys. Rev.*, vol. 74, pp. 235–239, Aug. 1948.

[9] K. S. Krane, *Introductory Nuclear Physics.* New York: Wiley, 1987.

[10] Y. Taniguchi, M. Kimura, Y. Kanada-En'yo, and H. Horiuchi, "Clustering and triaxial deformations of ^{40}Ca," *Phys. Rev. C*, vol. 76, p. 044317, Oct. 2007.

[11] T. Hartmann, J. Enders, P. Mohr, K. Vogt, S. Volz, and A. Zilges, "Dipole and electric quadrupole excitations in ^{40,48}Ca," *Phys. Rev. C*, vol. 65, p. 034301, Feb. 2002.

[12] M. Thoennessen, "Fusion-Evaporation Reactions," in *The Discovery of Isotopes: A Complete Compilation*, pp. 197–226, Cham: Springer International Publishing, 2016.

[13] G. J. Kumbartzki, N. Benczer-Koller, K.-H. Speidel, D. A. Torres, J. M. Allmond, P. Fallon, I. Abramovic, L. A. Bernstein, J. E. Bevins, H. L. Crawford, Z. E. Guevara, G. Gürdal, A. M. Hurst, L. Kirsch, T. A. Laplace, A. Lo, E. F. Matthews, I. Mayers, L. W. Phair, F. Ramirez, S. J. Q. Robinson, Y. Y. Sharon, and A. Wiens, "Z = 50

core stability in Sn 110 from magnetic-moment and lifetime measurements," *Physical Review C*, vol. 93, p. 044316, Apr. 2016.

[14] G. J. Kumbartzki, N. Benczer-Koller, S. Burcher, A. Ratkiewicz, S. L. Rice, Y. Y. Sharon, L. Zamick, K.-H. Speidel, D. A. Torres, K. Sieja, M. McCleskey, A. Cudd, M. Henry, A. Saastamoinen, M. Slater, A. Spiridon, S. Y. Torilov, V. I. Zherebchevsky, G. Gürdal, S. J. Q. Robinson, S. D. Pain, and J. T. Burke, "Transition from collectivity to single-particle degrees of freedom from magnetic moment measurements on 38 82 Sr 44 and 38 90 Sr 52," *Physical Review C*, vol. 89, p. 064305, June 2014.

[15] O. Kenn, K.-H. Speidel, R. Ernst, S. Schielke, S. Wagner, J. Gerber, P. Maier-Komor, and F. Nowacki, "Measurements of *g* factors and lifetimes of low-lying states in 62 – 70 Zn and their shell model implication," *Physical Review C*, vol. 65, p. 034308, Feb. 2002.

[16] D. A. Torres, G. J. Kumbartzki, Y. Y. Sharon, L. Zamick, B. Manning, N. Benczer-Koller, G. Gürdal, K.-H. Speidel, M. Hjorth-Jensen, P. Maier-Komor, S. J. Q. Robinson, T. Ahn, V. Anagnostatou, M. Elvers, P. Goddard, A. Heinz, G. Ilie, D. Radeck, D. Savran, and V. Werner, "First g -factor measurements of the 2 1 + and the 4 1 + states of radioactive 100 Pd," *Physical Review C*, vol. 84, p. 044327, Oct. 2011.

[17] L. G. Sobotka and V. E. Viola, "Nuclear Reactions," in *Handbook of Nuclear Chemistry* (A. Vértes, S. Nagy, Z. Klencsár, R. G. Lovas, and F. Rösch, eds.), pp. 143–221, Boston, MA: Springer US, 2011.

[18] H. Bateman, "Solution of a system of differential equations occurring in the theory of radioactive transformations," *Proceedings of the Cambridge Philosophical Society, Mathematical and physical sciences*, vol. 15, 1908.

[19] E. J. Williams, *Study of 28Mg and 22Ne using fusion-evaporation and Doppler shift techniques.* Thesis, Science: Department of Chemistry, Apr. 2019.

[20] G. F. Knoll, *Radiation detection and measurement: Glenn F. Knoll.* Wiley, 3rd ed. ed., 2000.

[21] P. Petkov, D. Tonev, J. Gableske, A. Dewald, and P. von Brentano, "Lifetime analysis using the Doppler-shift attenuation method with a gate on feeding transition," *Nuclear Instruments and Methods in Physics Research Section A: Accelerators, Spectrometers, Detectors and Associated Equipment*, vol. 437, pp. 274–281, Nov. 1999.

[22] W. Bothe, "Coincidence Method," *Science*, vol. 122, no. 3175, pp. 861–863, 1955. Publisher: American Association for the Advancement of Science.

[23] R. E. Laxdal and M. Marchetto, "The ISAC post-accelerator," *Hyperfine Interact*, vol. 225, pp. 79–97, Jan. 2014.

[24] J. Dilling, R. Krücken, and G. Ball, "ISAC overview," *Hyperfine Interact*, vol. 225, pp. 1–8, Jan. 2014.

[25] `https://electroweak.mines.edu/triumf-isac/`, Accessed: 2022-03-31.

[26] K. Jayamanna, F. Ames, G. Cojocaru, R. Baartman, P. Bricault, R. Dube, R. Laxdal, M. Marchetto, M. MacDonald, P. Schmor, G. Wight, and D. Yuan, "Off-line ion source terminal for ISAC at TRIUMF," *Review of Scientific Instruments*, vol. 79, p. 02C711, Feb. 2008. Publisher: American Institute of Physics.

[27] `https://grsi.wiki.triumf.ca/wiki/File:High_Efficiency_Mode.jpg`, Accessed: 2022-03-31.

[28] G. Hackman and C. E. Svensson, "The TRIUMF-ISAC gamma-ray escape suppressed specrometer, TIGRESS," *Hyperfine Interact*, vol. 225, pp. 241–251, Jan. 2014.

[29] P. Voss, R. Henderson, C. Andreoiu, R. Ashley, R. A. E. Austin, G. C. Ball, P. C. Bender, A. Bey, A. Cheeseman, A. Chester, D. S. Cross, T. E. Drake, A. B. Garnsworthy, G. Hackman, R. Holland, S. Ketelhut, P. Kowalski, R. Krücken, A. T. Laffoley, K. G. Leach, D. Miller, W. J. Mills, M. Moukaddam, C. J. Pearson, J. Pore, E. T. Rand, M. M. Rajabali, U. Rizwan, J. Shoults, K. Starosta, C. E. Svensson, E. Tardiff, C. Unsworth, K. Van Wieren, Z. M. Wang, and J. Williams, "The TIGRESS Integrated Plunger ancillary systems for electromagnetic transition rate studies at TRIUMF," *Nuclear Instruments and Methods in Physics Research Section A: Accelerators, Spectrometers, Detectors and Associated Equipment*, vol. 746, pp. 87–97, May 2014.

[30] P. Voss, R. Henderson, C. Andreoiu, R. Ashley, G. C. Ball, P. C. Bender, A. Chester, D. S. Cross, T. E. Drake, A. B. Garnsworthy, G. Hackman, S. Ketelhut, R. Krücken, D. Miller, M. M. Rajabali, K. Starosta, C. E. Svensson, E. Tardiff, C. Unsworth, and Z. M. Wang, "Digital Rise-Time Discrimination of Pulses from the Tigress Integrated Plunger Silicon PIN Diode Wall," *Physics Procedia*, vol. 66, pp. 524–531, Jan. 2015.

[31] J. P. Greene, P. J. Voss, and K. Starosta, "Thick backed carbon targets via mechanical rolling," *J Radioanal Nucl Chem*, vol. 299, pp. 1121–1124, Feb. 2014.

[32] J.-P. Martin, C. Mercier, N. Starinski, C. J. Pearson, and P.-A. Amaudruz, "The TIGRESS DAQ/Trigger System," *IEEE Transactions on Nuclear Science*, vol. 55, pp. 84–90, Feb. 2008. Conference Name: IEEE Transactions on Nuclear Science.

[33] `https://daq00.triumf.ca/MidasWiki/index.php/Event_Structure`, Accessed: 2022-04-07.

[34] S. Ritt, "The midas daq system," *Proc. 10th IEEE Real Time Conf. (Beaune)*, pp. 309–312.

[35] J. F. Ziegler, M. D. Ziegler, and J. P. Biersack, "SRIM – The stopping and range of ions in matter (2010)," *Nuclear Instruments and Methods in Physics Research Section B: Beam Interactions with Materials and Atoms*, vol. 268, pp. 1818–1823, June 2010.

[36] U. Rizwan, *Development of Gamma-Ray Spectroscopy Techniques for Fundamental and Applied Research*. Thesis, Science: Department of Chemistry, Sept. 2015.

[37] B. Mills, "Griffin efficiency calculator," Dec. 2015. `https://zenodo.org/record/35023`, Accessed: 2022-05-16.

[38] S. Agostinelli, J. Allison, K. Amako, J. Apostolakis, H. Araujo, P. Arce, M. Asai, D. Axen, S. Banerjee, G. Barrand, F. Behner, L. Bellagamba, J. Boudreau, L. Broglia, A. Brunengo, H. Burkhardt, S. Chauvie, J. Chuma, R. Chytracek, G. Cooperman, G. Cosmo, P. Degtyarenko, A. Dell'Acqua, G. Depaola, D. Dietrich, R. Enami, A. Feliciello, C. Ferguson, H. Fesefeldt, G. Folger, F. Foppiano, A. Forti, S. Garelli, S. Giani, R. Giannitrapani, D. Gibin, J. J. Gómez Cadenas, I. González, G. Gracia Abril, G. Greeniaus, W. Greiner, V. Grichine, A. Grossheim, S. Guatelli, P. Gumplinger, R. Hamatsu, K. Hashimoto, H. Hasui, A. Heikkinen, A. Howard, V. Ivanchenko, A. Johnson, F. W. Jones, J. Kallenbach, N. Kanaya, M. Kawabata, Y. Kawabata, M. Kawaguti, S. Kelner, P. Kent, A. Kimura, T. Kodama, R. Kokoulin, M. Kossov, H. Kurashige, E. Lamanna, T. Lampén, V. Lara, V. Lefebure, F. Lei, M. Liendl, W. Lockman, F. Longo, S. Magni, M. Maire, E. Medernach, K. Minamimoto, P. Mora de Freitas, Y. Morita, K. Murakami, M. Nagamatu, R. Nartallo, P. Nieminen, T. Nishimura, K. Ohtsubo, M. Okamura, S. O'Neale, Y. Oohata, K. Paech, J. Perl, A. Pfeiffer, M. G. Pia, F. Ranjard, A. Rybin, S. Sadilov, E. Di Salvo, G. Santin, T. Sasaki, N. Savvas, Y. Sawada, S. Scherer, S. Sei, V. Sirotenko, D. Smith, N. Starkov, H. Stoecker, J. Sulkimo, M. Takahata, S. Tanaka, E. Tcherniaev, E. Safai Tehrani, M. Tropeano, P. Truscott, H. Uno, L. Urban, P. Urban, M. Verderi, A. Walkden, W. Wander, H. Weber, J. P. Wellisch, T. Wenaus, D. C. Williams, D. Wright, T. Yamada, H. Yoshida, and D. Zschiesche, "Geant4-a simulation toolkit," *Nuclear Instruments and Methods in Physics Research Section A: Accelerators, Spectrometers, Detectors and Associated Equipment*, vol. 506, pp. 250–303, July 2003.

[39] R. Brun and F. Rademakers, "ROOT — An object oriented data analysis framework," *Nuclear Instruments and Methods in Physics Research Section A: Accelerators, Spectrometers, Detectors and Associated Equipment*, vol. 389, pp. 81–86, Apr. 1997.

[40] A. S. Chester, *Recoil distance method lifetime measurements of the 2_1^+ excited states in ^{84}Kr and ^{94}Sr.* Thesis, Science: Department of Chemistry, Dec. 2017.

[41] W. H. Press, B. P. Flannery, S. A. Teukolsky, and W. T. Vetterling, *Numerical Recipes in FORTRAN 77: The Art of Scientific Computing.* Cambridge University Press, 2 ed., Sept. 1992. Published: Hardcover.

[42] K. Olive, "Review of Particle Physics," *Chinese Physics C*, vol. 40, p. 100001, Oct. 2016.

[43] G. R. Choppin, J.-O. Liljenzin, and J. Rydberg, "CHAPTER 12 - Energetics of Nuclear Reactions," in *Radiochemistry and Nuclear Chemistry (Third Edition)* (G. R. Choppin, J.-O. Liljenzin, and J. Rydberg, eds.), pp. 334–347, Woburn: Butterworth-Heinemann, Jan. 2002.